

Copyright

by

Xiao Liu

2014

**The Thesis Committee for Xiao Liu  
Certifies that this is the approved version of the following thesis:**

**Computation of Near-Field Distribution around Wind Turbines**

**APPROVED BY  
SUPERVISING COMMITTEE:**

**Supervisor:**

---

Hao Ling

---

Ali E. Yilmaz

# **Computation of Near-Field Distribution around Wind Turbines**

**by**

**Xiao Liu, B.E.**

**Thesis**

Presented to the Faculty of the Graduate School of

The University of Texas at Austin

in Partial Fulfillment

of the Requirements

for the Degree of

**Master of Science in Engineering**

**The University of Texas at Austin**

**May 2014**

## **Acknowledgements**

I would like to take this opportunity to thank the people that inspired and guided me in this research. First, I would like to thank Dr. Hao Ling for his support and guidance. He spent numerous hours discussing with me about the possible directions and solutions. Second, I would like to thank Mr. Shang-Te Yang and Mr. Chenchen Li. They helped me a lot and provided a lot of useful suggestions to make this thesis possible. Third, I would like to thank Dr. Ali E. Yilmaz for his time and comments in reading this thesis.

Finally, I would like to thank my family for their support and encouragement these last two years.

## **Abstract**

### **Computation of Near-Field Distribution around Wind Turbines**

Xiao Liu, MSE

The University of Texas at Austin, 2014

Supervisor: Hao Ling

In this work, two approaches for computing the near-field distribution around wind turbines are proposed, including: (1) Huygens Principle and (2) the parabolic equation technique. In order to simplify the problem, the cylinder model is utilized to represent the wind turbines and transform the problem into a two-dimensional case. To make Huygens Principle computationally tractable, several approximations are made based on the problem geometry especially modelling the cylinder as a plate. The expression of the electromagnetic field radiated by the equivalent magnetic current can be analytically solved by the error function. To verify the results, FEKO is utilized to simulate the scattering of infinitely long cylinders using periodic boundary condition (PBC). In order to solve the problem of multiple cylinders, a modified method is derived. For more accurate results, the parabolic equation (PE) technique is utilized to solve this problem, which is usually utilized to solve wave propagation problems. In this case, wide-angle approximation is used to solve the parabolic equation, which can obtain accurate results in a region of up to 45 degrees. Although these two approaches are not full-wave simulation, the calculation time is significantly reduced and the error is

acceptable. To further verify the computed results by the parabolic equation technique, two commercial transceivers from Time Domain Corporation are used to measure the field distribution behind a finite-length metal pole. The frequency-domain results are obtained from the measured time-domain results using the fast Fourier transform. It is shown that the computed results by the parabolic equation technique agree well with the measurement results.

## Table of Contents

List of Tables .....	ix
List of Figures .....	x
Chapter 1: Introduction .....	1
Chapter 2: Huygens Principle Solution.....	4
Computation Region .....	4
Simplified Model .....	5
Equivalent Problem by Huygens Principle .....	7
TE Case.....	9
Error Function.....	13
TE Computed Results .....	13
Modified Equivalent Problem for TE .....	17
Solution to Problem of Two Plates .....	20
TM Case.....	23
TM Computed Results .....	24
Modified Equivalent Problem for TM.....	25
Backward Propagation Region .....	27
Comparison with Cylinder Model .....	28
Chapter 3: Parabolic Equation Solution.....	30
Introduction and Derivation.....	30
Standard Parabolic Equation.....	32
Wide-Angle Solution .....	33
Finite-Difference Implementation .....	34
Initial Vertical Plane .....	36
Boundary Condition (I).....	37
Boundary Condition (II) .....	38
Computed Results of Forward Propagation.....	40
Backward Propagation.....	44

Computed Results of Backward Propagation .....	46
Computation for Multiple Cylinders.....	47
Parabolic Equation Under Line Source Incidence .....	50
Chapter 4: Measurement Using UWB Transceivers.....	53
Transceiver and Channel Analysis Tool .....	53
Measurement.....	55
Data Processing.....	57
Results Comparison .....	57
Chapter 5: Conclusion.....	61
References.....	63

## List of Tables

Table 3.1: %RMS with different mesh size .....	44
Table 3.2: Coordinates of cylinders .....	48

## List of Figures

Figure 2.1: Forward and backward propagation region.....	4
Figure 2.2: Simplification of the Cylinder Model. ....	5
Figure 2.3: Scattering Width of PEC Plate and Cylinder along forward propagation direction. ....	6
Figure 2.4: Reflecting surfaces of different cross section.....	6
Figure 2.5: Huygens Principle.. ....	7
Figure 2.6: Construction of an equivalent problem. ....	8
Figure 2.7: Equivalent problem. ....	9
Figure 2.8: Equivalent problem for TE polarization.....	10
Figure 2.9: Radiation of an infinite magnetic line source.....	11
Figure 2.10: Amplitude of $E_x$ component for TE polarization. ....	14
Figure 2.11: Amplitude of $E_y$ component for TE polarization. ....	15
Figure 2.12: Problem of two plates.....	16
Figure 2.13: Modified equivalent problem for TE polarization. ....	18
Figure 2.14: Equivalent problem for TE-polarized plane wave without any scatterers. .....	18
Figure 2.15: Computed results for modified equivalent problem of TE polarization. .....	20
Figure 2.16: Modified equivalent problem of scattering for two plates (I) .....	21
Figure 2.17: Modified equivalent problem of scattering for two plates (II).....	22
Figure 2.18: Amplitude of $E_y$ component for two plates (TE). ....	22
Figure 2.19: Equivalent problem for TM polarization.....	23
Figure 2.20: Radiation of a magnetic current directed along y-axis.....	23

Figure 2.21: Amplitude of $E_z$ component for TM polarization. ....	25
Figure 2.22: Modified equivalent problem for TE.....	26
Figure 2.23: Radiation of a surface magnetic current oriented to y-direction .....	26
Figure 2.24: Computed results for modified equivalent problem of TM polarization. .....	27
Figure 2.25: Construction of equivalent problem for backward propagation region using Huygens Principle .....	28
Figure 2.26: Comparison between plate model and cylinder model. ....	29
Figure 3.1: The propagation directions constitute the paraxial zone .....	31
Figure 3.2: Crank-Nicolson finite-difference scheme. ....	35
Figure 3.3: Computed result at mesh size equal to $0.5\lambda$ .....	40
Figure 3.4: Computed result at mesh size equal to $0.25\lambda$ .....	41
Figure 3.5: Computed result at mesh size equal to $0.2\lambda$ .....	41
Figure 3.6: Computed result at mesh size equal to $0.1\lambda$ .....	42
Figure 3.7: Computed result at mesh size equal to $0.05\lambda$ .....	42
Figure 3.8: %RMS error with different mesh size.....	43
Figure 3.9: Facet Model.....	46
Figure 3.10: Computed result for backward propagation at mesh size equal to $0.01\lambda$ . .....	46
Figure 3.11: Simplified model of wind turbine farm.....	48
Figure 3.12: Scattering computation for a wind turbine farm. ....	49
Figure 3.13: Field distribution behind specific cylinders. ....	50
Figure 3.14: Field distribution under a line source incidence.....	51
Figure 4.1: Time Domain P410 UWB transceiver.....	54
Figure 4.2: Direct path and multipath.....	55

Figure 4.3: Measurement result by Channel Analysis Tool .....	55
Figure 4.4: Measurement Photos. ....	56
Figure 4.5: Scheme of measurement.....	56
Figure 4.6: Comparison between computation and measurement .....	59

## **Chapter 1: Introduction**

With the rapid development of wind energy as a non-polluting source all over the world, the adverse effect from wind turbines on radar and wireless communications systems is raising serious concerns [1-10]. New generation wind turbines are large structures that can interact significantly with electromagnetic waves. The reflecting surfaces include the spinning turbine blades, the nacelle, and the tower supporting them. A number of studies have been conducted on the following two topics – radar clutter and electromagnetic transmission interference. Wind turbine clutter is due to the backscattered signal from the turbines, in which the spinning turbine blades have an adverse effect on the detection of moving targets by a radar system. This topic has been well studied to date [11-15]. A less well-studied problem is the electromagnetic transmission interference due to blockage and multipath from wind turbine farm. It is well-known that there is a region behind a turbine structure where the scattered field destructively cancels with the incident field, which is called the shadow region. For a wireless communications system, the received signal strength decreases if the receiver is in the shadow region. The situation is similar for a radar system if the targets are in those regions. Outside the shadow region, the incident field and the scattered field interfere with each other constructively or destructively due to multipath, forming a rapid spatial oscillation, which also affects wireless systems.

Obviously, electromagnetic simulation software can be utilized to simulate the wind turbine farm and obtain the near-field distribution around it. However, full-wave simulation of a large wind farm by commercial software is usually time-consuming and has a large computational burden. Several studies have been conducted experimentally or theoretically on the characterization of the propagation interference problem. On one

hand, this problem can be studied by doing measurement directly [16, 17]. But the measurement problem involves a bistatic transmitter/receiver configuration which is more difficult to realize. On the other hand, numerical methods can be utilized. As shown in [3], a standard and simple computational methodology for estimating the shadow region can be derived based on the Fresnel zone argument. The radar cross section concept [18, 19] and physical optics method [20] have also been utilized. In [21], full-wave analysis is applied to analyze the shadow region. However, near-field computation with numerous sampling points is still computationally demanding.

In order to make this problem computationally tractable, a simplified model for this problem is needed. As shown in [22], for the transmission interference problem, several assumptions can be made, among which there are three important ones for further study. Firstly, the scattering of wind turbine is assumed to be dominated by the tower structure, compared to the blades and nacelle structures. Based on this assumption, we can use a perfectly conducting cylinder to model the wind turbine. Secondly, for the turbine whose height is much larger than the cross section, the scattering process can be assumed to be a two-dimensional case for observers close to the turbine. Finally, the individual turbines are assumed to be excited under the incident excitation while neglecting the interactions from others. Based on these assumptions, the original propagation problem becomes a two-dimensional scattering problem of multiple cylinders with infinite length. By utilizing the cylinder model, the computation of the near-field distribution is simplified, which makes the fast computation of this scattering problem possible.

In this thesis, two approaches based on the simplified model above are proposed. The first one is to utilize Huygens Principle for this problem and derive a corresponding analytical solution using the error function. In this method, the model is simplified further

in order to make Huygens Principle computationally tractable. To verify the computation results, the commercial electromagnetic package FEKO [23] is used. For more accurate computation results, a second approach based on the parabolic equation technique is implemented. A wide-angle approximation is used for solving the equations and perfectly absorbing layers are selected as the boundary condition to truncate the computation region. The near-field distribution around an infinitely long PEC cylinder is obtained. In addition to verification by FEKO simulation, we also utilize the Channel Analysis Tool of the transceiver designed by Time Domain Corporation to measure the field distribution behind a metal pole.

The thesis is organized as follows. In Chapter 2, the cylinder model is further simplified to the plate model. The equivalent problem is constructed from Huygens Principle and the analytical solution is derived using the error function. Simulation in FEKO is done to verify the results. In Chapter 3, the parabolic equation technique is discussed and utilized for the wind turbine problem. The forward and backward propagation is discussed respectively. The scattering computation of a cylinder under the incidence of an infinitely long line source by the parabolic equation technique is also derived. In Chapter 4, in order to verify the computed results from the parabolic equation technique, measurement of a metal pole is done by using two commercial transceivers from Time Domain Corporation. The result is compared with that from the parabolic equation technique. Finally, Chapter 5 concludes this work and discusses potential future work.

## Chapter 2: Huygens Principle Solution

As is shown in [22], the three-dimensional propagation interference problem of a wind turbine can be simplified to the two-dimensional scattering problem of a cylinder, which is much easier to be solved by numerical methods. In this chapter, we will first simplify the cylinder model further to a plate model and construct an equivalent problem by using Huygens Principle. Then, by using the error function, the analytical solution of this problem can be obtained. This method can also be modified and tailored for the multiple turbine problem. The computed results from this approach are compared with the results from FEKO simulation.

### COMPUTATION REGION

First, the computation region is divided into two parts according to the position of the cylinder and the direction of the incident wave, as is shown in Figure 2.1. The region ahead of the cylinder is called the backward propagation region while the one behind the cylinder is called the forward propagation region. For a cylinder centered at  $(0,0)$  and an incident wave propagating along the positive  $x$ -axis, the forward propagation region is where  $x > 0$  while the backward region is where  $x < 0$ .

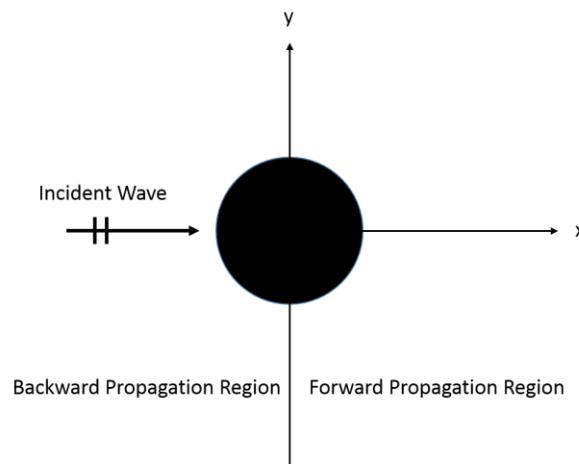


Figure 2.1: Forward and backward propagation region.

## SIMPLIFIED MODEL

The original problem is shown in Figure 2.2(a), which is a two-dimensional scattering problem of an infinite-length PEC cylinder with a diameter of  $a$ . In order to use Huygens Principle to construct an equivalent problem which is computationally tractable, we need to make a few approximations to simplify this problem further. First, we simplify the circular cross section of the cylinder as a strip whose width is equal to  $a$ , with infinitesimal thickness, as shown in Figure 2.2(b). Then, the infinite-length PEC cylinder in the original problem is simplified into an infinite-length plate.

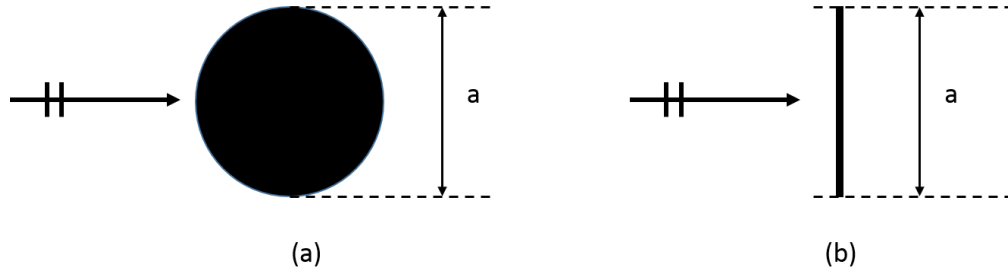


Figure 2.2: Simplification of the Cylinder Model. (a) Original Model. (b) Simplified Model

As shown in [24], along the forward propagation direction (the positive  $x$ -direction here), the scattering width of a PEC plate with a width of  $a$  can be expressed as

$$\sigma_{2D-plate} = \frac{2\pi a^2}{\lambda} \quad (2-1)$$

while the one of a PEC cylinder with a diameter of  $a$  is

$$\sigma_{2D-cylinder} = \frac{4}{k_0} \left| \sum_{-\infty}^{+\infty} \frac{J_n(k_0 a / 2)}{H_n^{(2)}(k_0 a / 2)} \right|^2 \quad (2-2)$$

where  $k_0$  is the wavenumber in free space. As is shown in Figure 2.3 (in dB scale), when  $k_0 a$  is increased, the difference of scattering width along forward propagation direction

between plate and cylinder becomes smaller. Thus, here we assume that the electromagnetic field in the forward propagation region of the plate is almost the same as the cylinder. According to geometrical optics, this is not a good approximation for the backward propagation region since the reflecting facets are different, as shown in Figure 2.4.

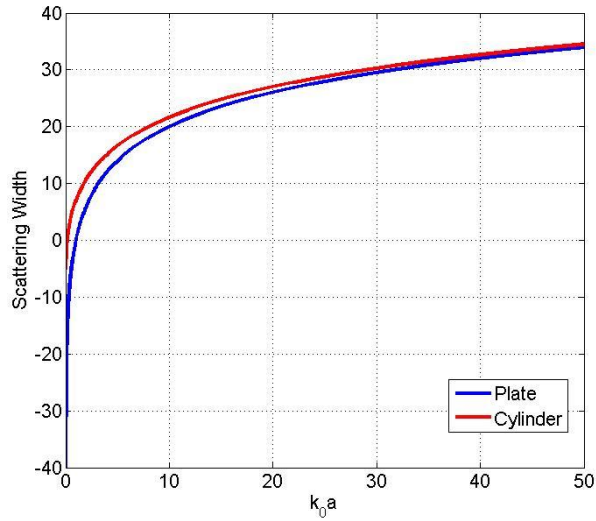


Figure 2.3: Scattering Width of PEC Plate and Cylinder along forward propagation direction.

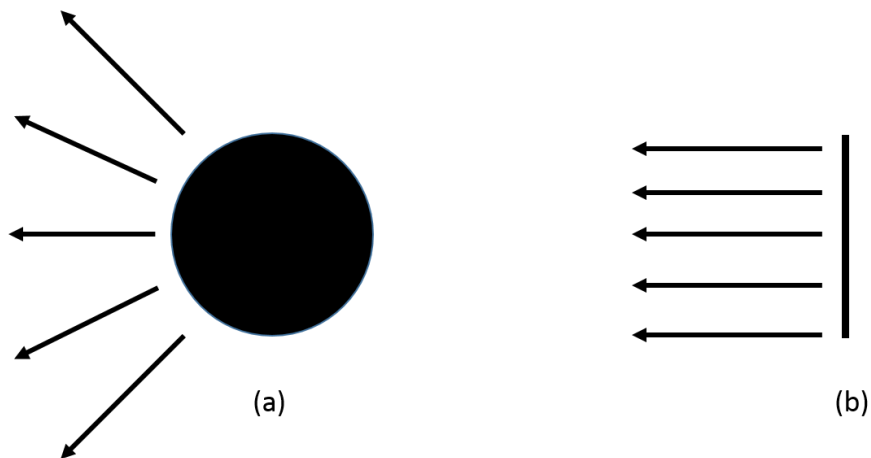


Figure 2.4: Reflecting surfaces of different cross section. (a) Cylinder. (b) Plate.

## EQUIVALENT PROBLEM BY HUYGENS PRINCIPLE

Using the above approximation, the original problem becomes a two-dimensional scattering problem of a PEC plate, which is infinitely long along the z-axis, as shown in Figure 2.5(a). We are interested in the region on the right side of y-axis. First, we draw an equivalent surface  $\Sigma$  along y-axis and remove the impressed source (as the incident plane wave here), as shown in Figure 2.5(b). Along the imaginary surface  $\Sigma$  there must exist the equivalent sources

$$\vec{J}_s = \hat{n} \times (\vec{H}_2 - \vec{H}_1) \quad (2-3)$$

$$\vec{M}_s = (\vec{E}_2 - \vec{E}_1) \times \hat{n} \quad (2-4)$$

Since we are not interested in the region on the left side of  $\Sigma$ , we assume the field in that region is zero. On the right side,  $\vec{E}_2$  and  $\vec{H}_2$  are the fields we want to compute, which are equal to  $\vec{E}$  and  $\vec{H}$  in Figure 2.5(a). It is well-known that the tangential electric field along the PEC plate is zero, so along the plate the equivalent magnetic current is zero, as shown in Figure 2.5(b).

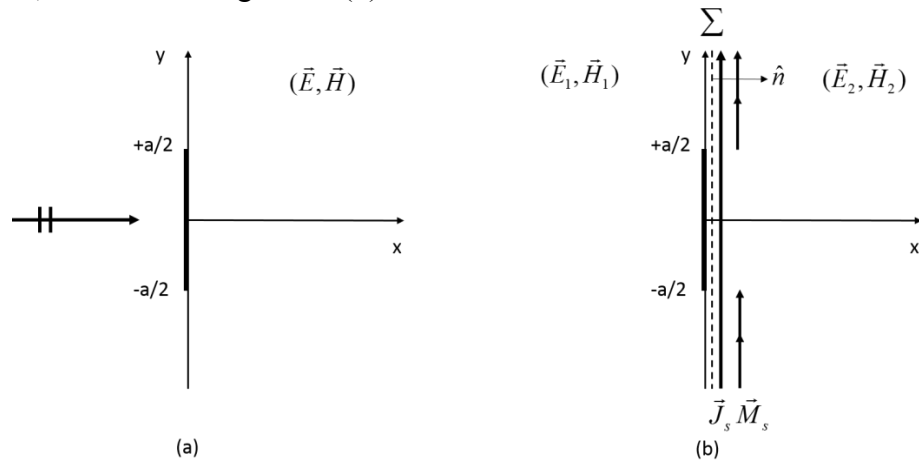


Figure 2.5: Huygens Principle. (a) Original problem. (b) Equivalent problem.

Then the equivalent problem in Figure 2.5(b) reduces to that of Figure 2.6(a) with equivalent current densities equal to

$$\vec{J}_s = \hat{n} \times \vec{H} \quad (2-5)$$

$$\vec{M}_s = \vec{E} \times \hat{n} \quad (2-6)$$

Since on the left side of  $\Sigma$  the field is zero everywhere, we fill that region with infinitely large PEC plane, as shown in Figure 2.6(b). Using image theory, the equivalent problem becomes that of Figure 2.6(c).

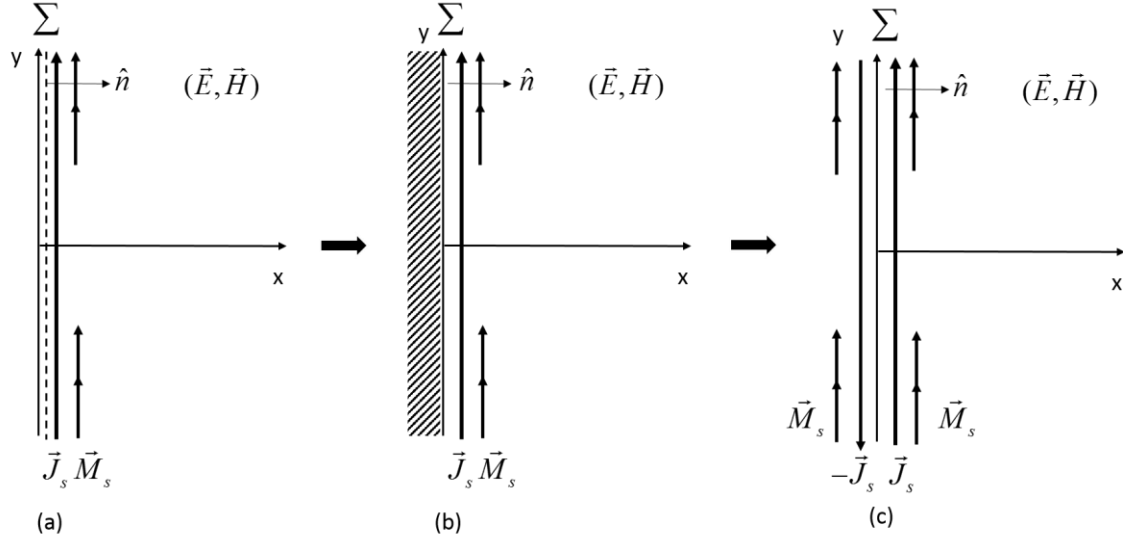


Figure 2.6: Construction of an equivalent problem.

Thus, the problem in Figure 2.5(a) reduces to that of Figure 2.7, where

$$\vec{M}_s = 2\vec{E} \times \hat{n} \quad (2-7)$$

in which  $\vec{M}_s$  is divided into two parts, one starts from  $y=a/2$  and extends to positive infinity while the other one starts from  $y=-a/2$  and extends to negative infinity, as shown in Figure 2.7.

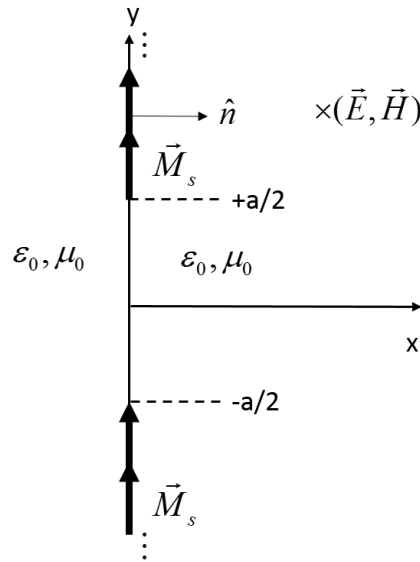


Figure 2.7: Equivalent problem.

The next step is to compute the radiation of the magnetic surface current for region  $x > 0$ . As is shown, the direction of  $\vec{M}_s$  is related to the total field at  $\Sigma$ . We assume that along the surface  $\Sigma$  the total field is equal to the incident field (except the region between  $-a/2$  and  $a/2$ )

$$\vec{E}|_{x=0} \approx \vec{E}_{in}|_{x=0} \quad (2-8)$$

Then the equivalent magnetic current is related to the incident electric field, whose direction is decided by the polarization of the incident field. The problem will be discussed in two cases respectively: TE polarization and TM polarization.

### TE CASE

For an incident plane wave of TE-polarization, the direction of equivalent magnetic current is along z-axis, as shown in Figure 2.8.

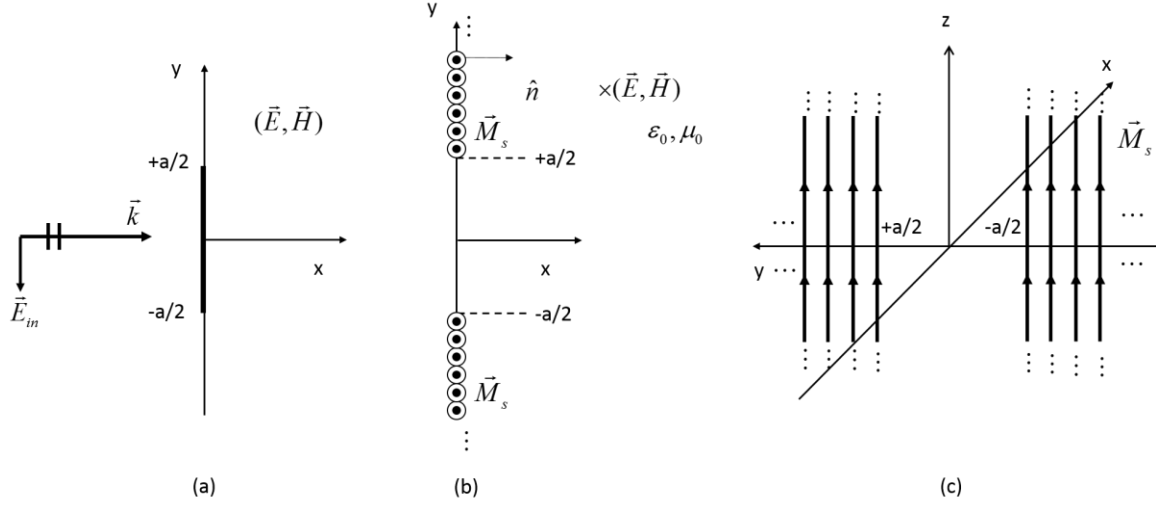


Figure 2.8: Equivalent problem for TE polarization. (a) Original Problem. (b)&(c) Equivalent problem

It should be noted that  $\vec{M}_s$  is infinitely long in  $z$  direction (as shown in Figure 2.8(c)). Thus, the electric field radiated by an infinitely long magnetic current along  $z$ -axis is given by [24]

$$E_\phi = +jI_m \frac{k_0}{4} H_1^{(2)}(k_0 \rho) \stackrel{far\ field}{\approx} -I_m \sqrt{\frac{jk_0}{8\pi}} \frac{e^{-jk_0 \rho}}{\sqrt{\rho}} \quad (2-9)$$

Therefore the electric field at point  $(x,y)$  radiated by an infinitely long magnetic current  $I_m$  located at  $(0,y')$  (as shown in Figure 2.9) can be expressed as

$$E_\phi = -I_m \sqrt{\frac{jk_0}{8\pi}} \frac{\exp(-jk_0 \sqrt{x^2 + (y-y')^2})}{\sqrt{x^2 + (y-y')^2}} \quad (2-10)$$

The electric field in Cartesian coordinates can be expressed as

$$E_x = -E_\phi \frac{y-y'}{\sqrt{x^2 + (y-y')^2}} = +I_m \sqrt{\frac{jk_0}{8\pi}} \frac{\exp(-jk_0 \sqrt{x^2 + (y-y')^2})}{(x^2 + (y-y')^2)^{\frac{3}{4}}} (y-y') \quad (2-11)$$

$$E_y = +E_\phi \frac{x}{\sqrt{x^2 + (y-y')^2}} = -I_m \sqrt{\frac{jk_0}{8\pi}} \frac{\exp(-jk_0 \sqrt{x^2 + (y-y')^2})}{(x^2 + (y-y')^2)^{\frac{3}{4}}} x \quad (2-12)$$

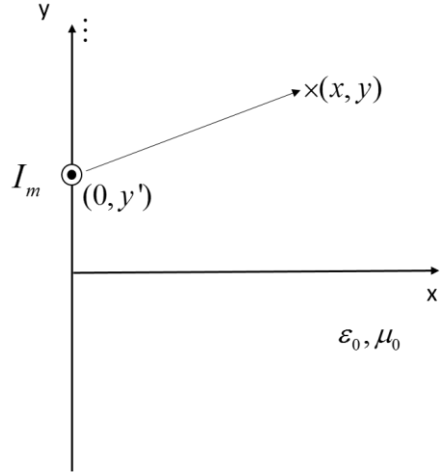


Figure 2.9: Radiation of an infinite magnetic line source

In order to simplify the expression of the field, we make two approximations:

(1) Using Taylor expansion to express the square-root term in the numerator

$$\rho = \sqrt{x^2 + (y - y')^2} \approx x + \frac{(y - y')^2}{2x} \quad (2-13)$$

while the error is zero at  $y' = y$ . This approximation only generates errors in phase.

(2) For the denominator, assume that

$$x^2 + (y - y')^2 \approx x^2 \quad (2-14)$$

which is also accurate when  $y' = y$ . We make this approximation in order to make the denominator a constant when computing the field at point  $(x, y)$ . The error becomes larger when  $|y' - y|$  is larger. However, when  $y'$  is far away from  $y$ , the contribution from that current is small, we will see later that this error is acceptable. By applying the approximations, the Eqn. 2-11 and 2-12 yield

$$E_x = +I_m \sqrt{\frac{jk_0}{8\pi}} \frac{\exp(-jk_0(x + \frac{1}{2x}(y - y')^2))}{x^{\frac{3}{2}}} (y - y') \quad (2-15)$$

$$E_y = -I_m \sqrt{\frac{jk_0}{8\pi}} \frac{\exp(-jk_0(x + \frac{1}{2x}(y - y')^2))}{\sqrt{x}} \quad (2-16)$$

Assume the incident electric field is equal to

$$\vec{E}_{in} = -\exp(-jk_0x)\hat{y} \quad (2-17)$$

Then  $\vec{M}_s$  can be expressed as

$$\vec{M}_s = 2\vec{E}_{in}|_{x=0} \times \hat{n} = 2\hat{z} \quad (2-18)$$

Then

$$E_x = +2\sqrt{\frac{jk_0}{8\pi}} \frac{\exp(-jk_0(x + \frac{1}{2x}(y-y')^2))}{x^{\frac{3}{2}}} (y-y') \quad (2-19)$$

$$E_y = -2\sqrt{\frac{jk_0}{8\pi}} \frac{\exp(-jk_0(x + \frac{1}{2x}(y-y')^2))}{\sqrt{x}} \quad (2-20)$$

Since the total electric field at point (x,y) is equal to the sum of field radiated by  $I_m$  located at different positions, it can be expressed as an integral at  $(-\infty, -a/2) \cup (a/2, +\infty)$ , as shown below

$$\begin{aligned} E_x(x, y) &= +2\sqrt{\frac{jk_0}{8\pi}} \left( \int_{-\infty}^{-\frac{a}{2}} \frac{\exp(-jk_0(x + \frac{1}{2x}(y-y')^2))}{x^{\frac{3}{2}}} (y-y') dy' + \int_{+\frac{a}{2}}^{+\infty} \frac{\exp(-jk_0(x + \frac{1}{2x}(y-y')^2))}{x^{\frac{3}{2}}} (y-y') dy' \right) \quad (2-21) \\ &= +2\sqrt{\frac{jk_0}{8\pi}} \frac{\exp(-jk_0(x + \frac{y^2}{2x}))}{x^{\frac{3}{2}}} \left( y \int_{-\infty}^{-\frac{a}{2}} \exp(-Ay'^2 + By') dy' + y \int_{+\frac{a}{2}}^{+\infty} \exp(-Ay'^2 + By') dy' \right. \\ &\quad \left. - \int_{-\infty}^{-\frac{a}{2}} y' \exp(-Ay'^2 + By') dy' - \int_{+\frac{a}{2}}^{+\infty} y' \exp(-Ay'^2 + By') dy' \right) \end{aligned}$$

$$\begin{aligned} E_y(x, y) &= -2\sqrt{\frac{jk_0}{8\pi}} \left( \int_{-\infty}^{-\frac{a}{2}} \frac{\exp(-jk_0(x + \frac{1}{2x}(y-y')^2))}{\sqrt{x}} dy' + \int_{+\frac{a}{2}}^{+\infty} \frac{\exp(-jk_0(x + \frac{1}{2x}(y-y')^2))}{\sqrt{x}} dy' \right) \quad (2-22) \\ &= -2\sqrt{\frac{jk_0}{8\pi}} \frac{\exp(-jk_0(x + \frac{y^2}{2x}))}{\sqrt{x}} \left( \int_{-\infty}^{-\frac{a}{2}} \exp(-Ay'^2 + By') dy' + \int_{+\frac{a}{2}}^{+\infty} \exp(-Ay'^2 + By') dy' \right) \end{aligned}$$

where  $A = \frac{jk_0}{2x}$ ,  $B = \frac{jk_0y}{x}$ .

## ERROR FUNCTION

In order to compute the field, we need to give a solution of the integral term. Obviously, we can use a brute-force integration to get the numerical solution. But we can also obtain the analytical solution of the integral faster by using the error function. The analytical solution of the integrals used here can be expressed as

$$\int_{-\infty}^X \exp(-Ax^2 + Bx)dx = \frac{1}{2\sqrt{A}} \sqrt{\pi} \exp\left(\frac{B^2}{4A}\right) \left(1 - \text{Erf}\left(\frac{B-2AX}{2\sqrt{A}}\right)\right) \quad (2-23)$$

$$\int_X^{+\infty} \exp(-Ax^2 + Bx)dx = \frac{1}{2\sqrt{A}} \sqrt{\pi} \exp\left(\frac{B^2}{4A}\right) \left(1 - \text{Erf}\left(\frac{2AX-B}{2\sqrt{A}}\right)\right) \quad (2-24)$$

$$\int_{-\infty}^X x \exp(-Ax^2 + Bx)dx = \frac{1}{4A^{\frac{3}{2}}} (-2\sqrt{A} \exp(X(B-AX)) + B\sqrt{\pi} \exp\left(\frac{B^2}{4A}\right) (1 - \text{Erf}\left(\frac{B-2AX}{2\sqrt{A}}\right))) \quad (2-25)$$

$$\int_X^{+\infty} x \exp(-Ax^2 + Bx)dx = \frac{1}{4A^{\frac{3}{2}}} (2\sqrt{A} \exp(X(B-AX)) + B\sqrt{\pi} \exp\left(\frac{B^2}{4A}\right) (1 + \text{Erf}\left(\frac{B-2AX}{2\sqrt{A}}\right))) \quad (2-26)$$

where  $\text{Erf}(x)$  is the error function defined as

$$\text{Erf}(x) = \frac{2}{\sqrt{\pi}} \int_0^x \exp(-t^2)dt \quad (2-27)$$

which can be solve by numerical software such as MATLAB. Then we can obtain the solution of electric field at point (x,y) for the TE polarization.

## TE COMPUTED RESULTS

Using the method above, we compute the scattering of a PEC plate located at (0,0) with a width of 4 meters under a TE-polarized incident wave at 500MHz and compare the results with the simulation of the same PEC plate by FEKO. The results are shown in Figure 2.10 and 2.11 (in dB scale) where the error is defined as

$$\text{Error} = 20 \log_{10} \left( \frac{\| |E_{com}| - |E_{sim}| \|}{|E_{in}|} \right) \quad (2-28)$$

where  $E_{com}$  is the computed result by using the method above,  $E_{sim}$  is the simulation result from FEKO and  $E_{in}$  is the incident field whose amplitude is equal to one in this case. Thus, the error here compares the difference between the computed result and simulation result, normalized by the strength of the incident field.

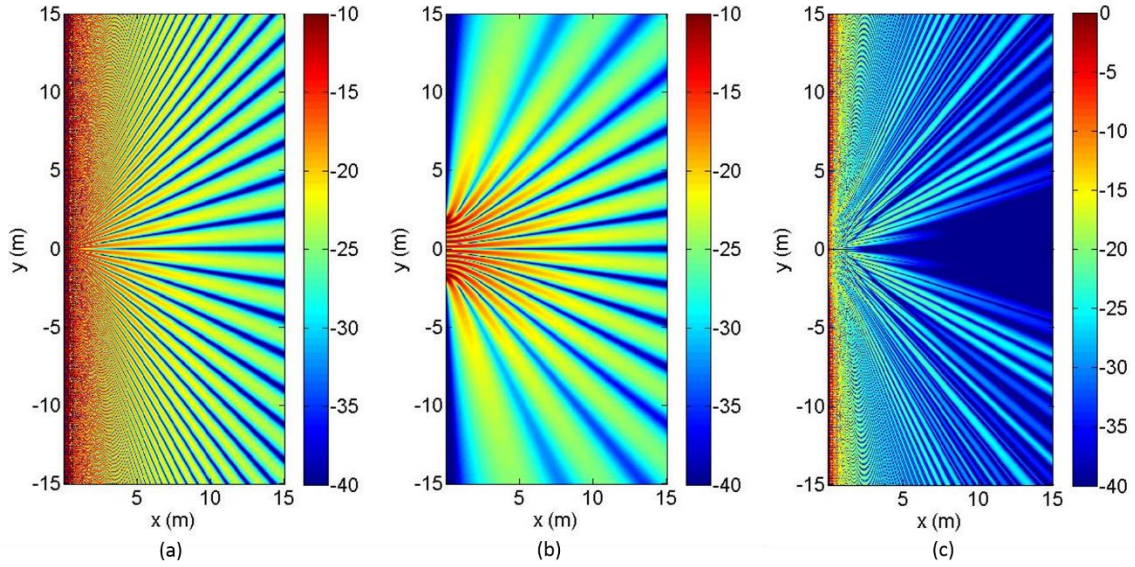


Figure 2.10: Amplitude of  $E_x$  component for TE polarization. (a) Computed result by Huygens Principle. (b) Simulation result by FEKO. (c) Error

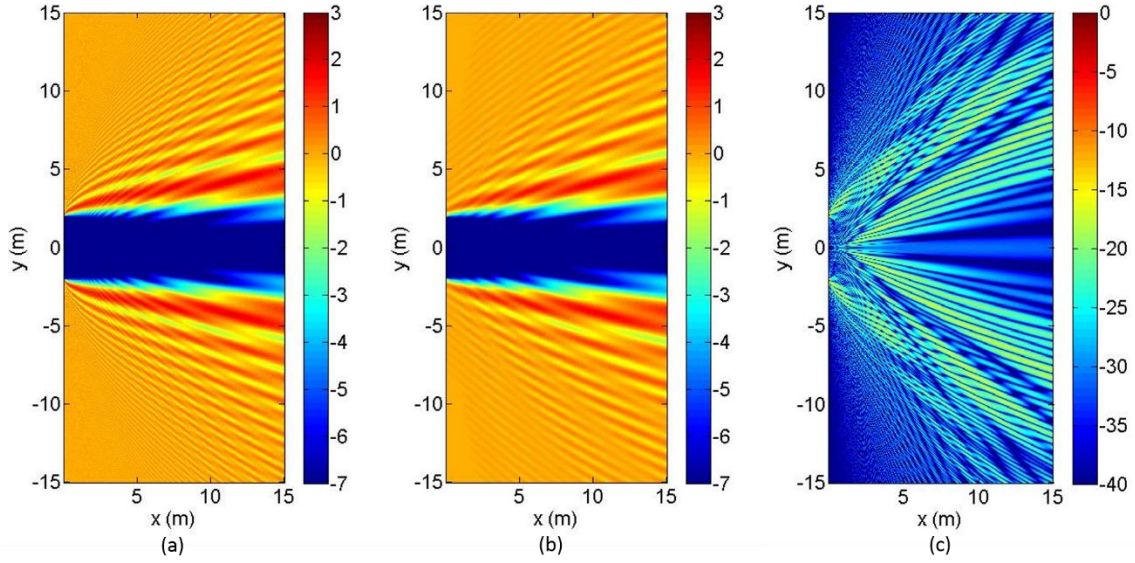


Figure 2.11: Amplitude of  $E_y$  component for TE polarization. (a) Computed result by Huygens Principle. (b) Simulation result by FEKO. (c) Error

It is shown that compared with  $E_y$ , the amplitude of  $E_x$  is pretty small and can be neglected when computing the total field. For both  $E_x$  and  $E_y$ , the error is less than -20dB almost over the entire region when compared with the incident field.

As shown before, there are several approximations made to simplify the original question:

- (1) Approximate the cylinder as a plate
- (2) Assume the total electric field  $\vec{E}$  at  $x=0$  is equal to the incident field  $\vec{E}_{inc}$
- (3) Use the far-field solution of an infinitely long magnetic current to compute the near-field region
- (4) Use Taylor expansion to express  $\rho$  in the numerator
- (5) Use x-coordinate of observation point to approximate  $\rho$  in the denominator

Due to the second approximation made here, the equivalent magnetic current is a constant at  $y \in (-\infty, -a/2) \cup (+a/2, +\infty)$ . In other words, we know the expression of the

current and then solve the problem using the method above. However, if we cannot obtain the expression of equivalent current, this method does not work. For example, as shown in Figure 2.12(a), there are two plates located at different position. The first is still located at  $(0,0)$  while the second one is at  $(x',y')$ . Assume the region between  $0$  and  $x'$  is called Region 1 and the region where  $x > x'$  is Region 2. If we are interested in the field of Region 2, we can draw the equivalent magnetic current along  $x=x'$ . It can be found that some part of  $\vec{M}_s$  is in the shadow region of the first plate. Although we can assume the second plate has no influence on the field along  $x=x'$  (except where it is located) and compute the field using the method above, the expression of equivalent current along  $x=x'$  already has a term including the error function. We cannot obtain an analytical solution of it so this method cannot be used.

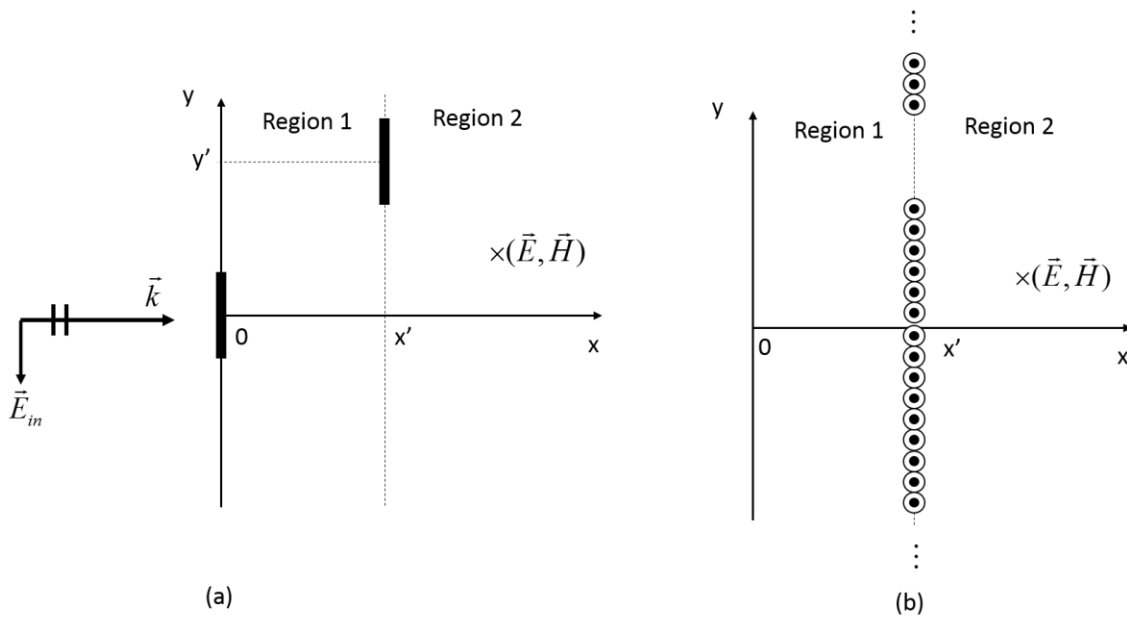


Figure 2.12: Problem of two plates. (a) Original problem. (b) Equivalent problem.

## MODIFIED EQUIVALENT PROBLEM FOR TE

As is shown, the method derived above cannot solve the scattering problem of multiple plates. In order to solve this problem, a modified method is needed to compute the field by using the error function in which the exact expression of the equivalent current in the shadow region is not required. We derive this modified method starting from the one-plate case shown in Figure 2.8(a). The scheme of the method we used above is shown in Figure 2.13(a), where the infinitely long equivalent magnetic current is distributed along  $y \in (-\infty, -a/2) \cup (+a/2, +\infty)$ . As is shown, it can be regarded as a combination of the radiation problem shown in Figure 2.13(b) and Figure 2.13(c). In Figure 2.12(b), the magnetic current in the same direction is distributed along  $y \in (-\infty, +\infty)$  while the current in Figure 2.13(c) is distributed along  $y \in (-a/2, +a/2)$  and it is in the opposite direction. Since the current shown in Figure 2.12(a) is equal to the sum of the currents in Figure 2.13(b) and Figure 2.13(c), the original equivalent current in Figure 2.13(a) can be replaced. And then the field we are interested in can be expressed as the sum of the fields generated by the new equivalent currents

$$\vec{E} = \vec{E}_1 + \vec{E}_2 \quad (2-29)$$

It can be shown that the problem of Figure 2.13(b) is just an equivalent problem of the case where the width of plate is equal to zero. In other words, there is only an incident wave without any scatterers as shown in Figure 2.14(a). Therefore the electric field  $\vec{E}_1$  is equal to the incident field

$$\vec{E}_1 = \vec{E}_m = -\hat{y} \exp(-jk_0 x) \quad (2-30)$$

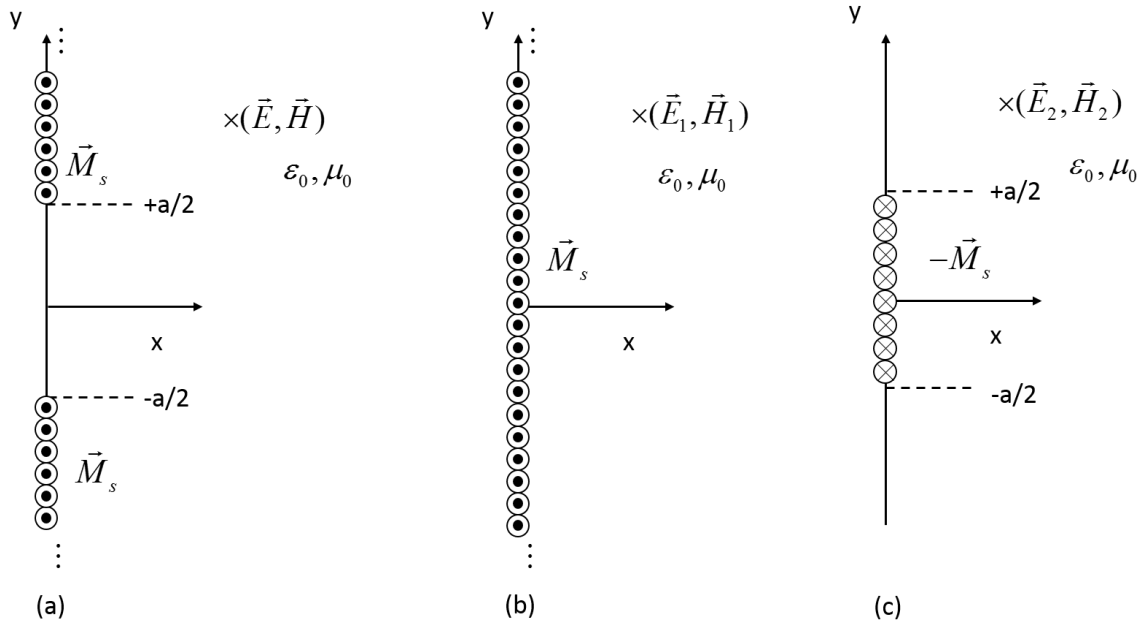


Figure 2.13: Modified equivalent problem for TE polarization. (a) Original equivalent problem. (b)&(c) Modified equivalent problem.

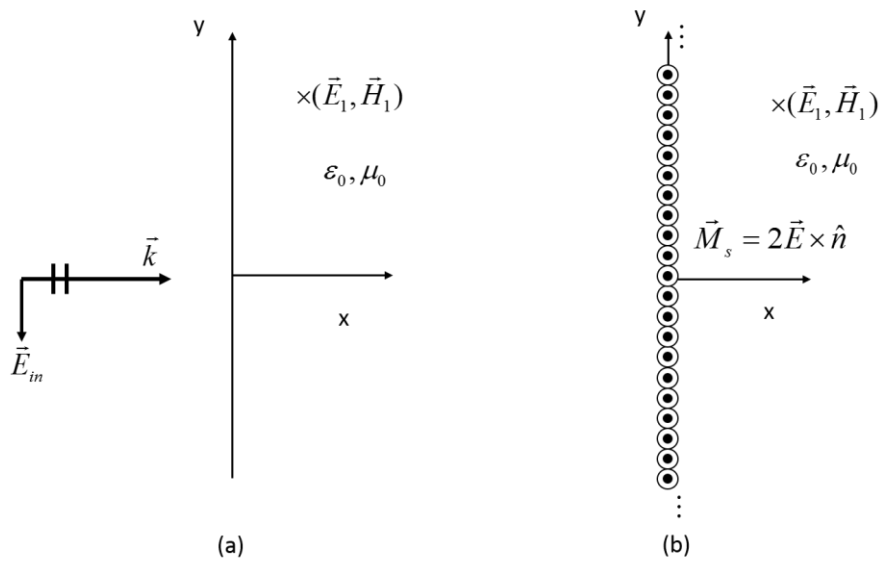


Figure 2.14: Equivalent problem for TE-polarized plane wave without any scatterers. (a) Original problem. (b) Equivalent problem.

For the electric field  $\vec{E}_2$ , it can be expressed as

$$E_{2x}(x, y) = -2\sqrt{\frac{jk_0}{8\pi}} \frac{\exp(-jk_0(x + \frac{y^2}{2x}))}{x^{\frac{3}{2}}} (y \int_{-\frac{a}{2}}^{+\frac{a}{2}} \exp(-Ay'^2 + By') dy' - \int_{-\frac{a}{2}}^{+\frac{a}{2}} y' \exp(-Ay'^2 + By') dy') \quad (2-31)$$

$$E_{2y}(x, y) = +2\sqrt{\frac{jk_0}{8\pi}} \frac{\exp(-jk_0(x + \frac{y^2}{2x}))}{\sqrt{x}} (\int_{-\frac{a}{2}}^{+\frac{a}{2}} \exp(-Ay'^2 + By') dy') \quad (2-32)$$

where  $A = \frac{jk_0}{2x}$ ,  $B = \frac{jk_0 y}{x}$ .

And the integrals used here can also be solved by the error function

$$\int_{X_1}^{X_2} \exp(-Ax^2 + Bx) dx = -\frac{\sqrt{\pi} \exp(\frac{B^2}{4A}) (Erf(\frac{-B + 2AX_1}{2\sqrt{A}}) + Erf(\frac{B - 2AX_2}{2\sqrt{A}}))}{2\sqrt{A}} \quad (2-33)$$

$$\int_{X_1}^{X_2} x \exp(-Ax^2 + Bx) dx = \frac{1}{4A^{\frac{3}{2}}} (2\sqrt{A} (\exp(X_1(B - AX_1)) - \exp(X_2(B - AX_2)))) \quad (2-34)$$

$$+ B\sqrt{\pi} \exp(\frac{B^2}{4A}) (Erf(\frac{B - 2AX_1}{2\sqrt{A}}) + Erf(\frac{-B + 2AX_2}{2\sqrt{A}}))$$

And then the total field can be expressed as

$$E_x(x, y) = -2\sqrt{\frac{jk_0}{8\pi}} \frac{\exp(-jk_0(x + \frac{y^2}{2x}))}{x^{\frac{3}{2}}} (y \int_{-\frac{a}{2}}^{+\frac{a}{2}} \exp(-Ay'^2 + By') dy' - \int_{-\frac{a}{2}}^{+\frac{a}{2}} y' \exp(-Ay'^2 + By') dy') \quad (2-35)$$

$$E_y(x, y) = -\exp(jk_0 x) + 2\sqrt{\frac{jk_0}{8\pi}} \frac{\exp(-jk_0(x + \frac{y^2}{2x}))}{\sqrt{x}} (\int_{-\frac{a}{2}}^{+\frac{a}{2}} \exp(-Ay'^2 + By') dy') \quad (2-36)$$

which can obtain the same answer as the scheme shown in Figure 2.7, which is shown in Figure 2.15

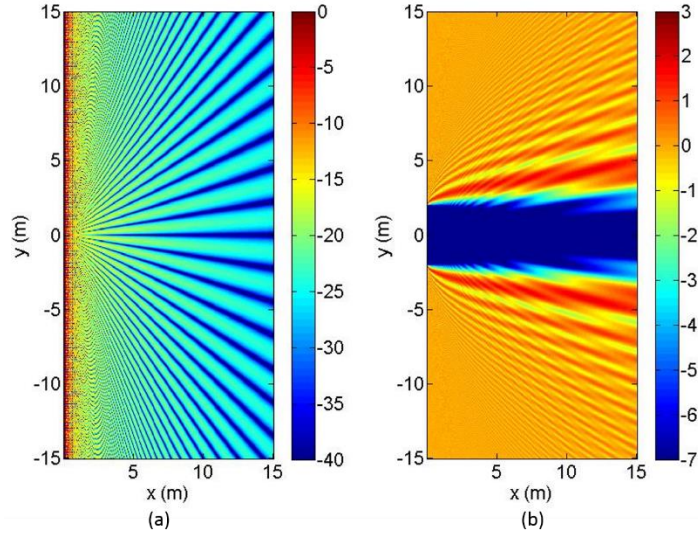


Figure 2.15: Computed results for modified equivalent problem of TE polarization. (a)  $E_x$  component. (b)  $E_y$  component.

### SOLUTION TO PROBLEM OF TWO PLATES

Using this modified method, we can solve the two-plate problem shown in Figure 2.12(a). As is shown, it is equal to the combination of Figure 2.16(a) and (b). The electric field we are interested in at Region 2 can be expressed as  $\vec{E} = \vec{E}_1 + \vec{E}_2$ , where  $\vec{E}_1$  is radiated by the infinitely long magnetic current in Figure 2.16(a) and  $\vec{E}_2$  is radiated by the finite magnetic current in Figure 2.16(b). If we assume the effect on the field along  $x=x'$  from the second plate is pretty small, then Figure 2.16(a) is just an equivalent problem of Figure 2.17(a). As is shown, there is only one plate located at (0,0) and we want to solve the electric field  $\vec{E}_1$  in Figure 2.17(a). Using the method shown in Figure 2.13, we can get that

$$\vec{E}_1 = -\hat{y} \exp(-jk_0 x) + \vec{E}_3 \quad (2-37)$$

where  $\vec{E}_3$  is the electric field due to the magnetic current  $-\vec{M}'_s$  in Figure 2.17(b). Then the electric field in Region 2 of Figure 2.12(a) can be expressed as

$$\vec{E} = -\hat{y} \exp(-jk_0 x) + \vec{E}_3 + \vec{E}_2 \quad (2-38)$$

where  $\vec{E}_2$  is radiated by the equivalent magnetic current  $-\vec{M}_s$  in Figure 2.16(b). If the two plates are far away from each other in y-direction, we can assume that the equivalent current in Figure 2.16(b) can be expressed by the incident field

$$\vec{M}_s \approx 2\vec{E}_{in}|_{x=x'} \times \hat{n} = 2 \exp(-jk_0 x') \hat{z} \quad (2-39)$$

In other words, this approximation is only suitable for problems in which the second plate is far away from the shadow region of the first one. If the second plate is in or close to the shadow region, the method we use here is not suitable. Figure 2.18 shows the computed result of  $E_y$  component for the two-plate case. The first plate is located at (0,-100m) while the second is at (200m,100m). Both of them have a width of 4 meters. It is shown that the result by Huygens Principle is good except for the region ahead of the second cylinder, which is due to the backward propagation scatter field we do not consider here.

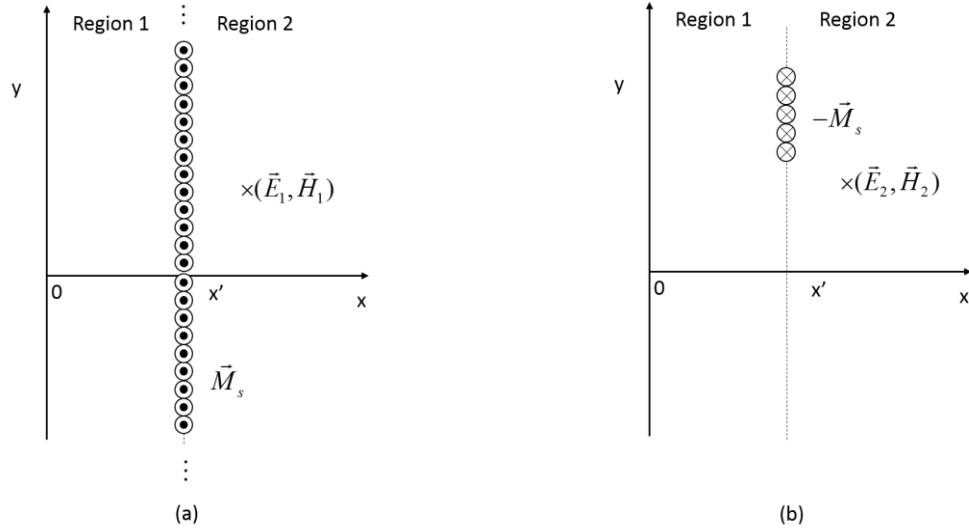


Figure 2.16: Modified equivalent problem of scattering for two plates (I)

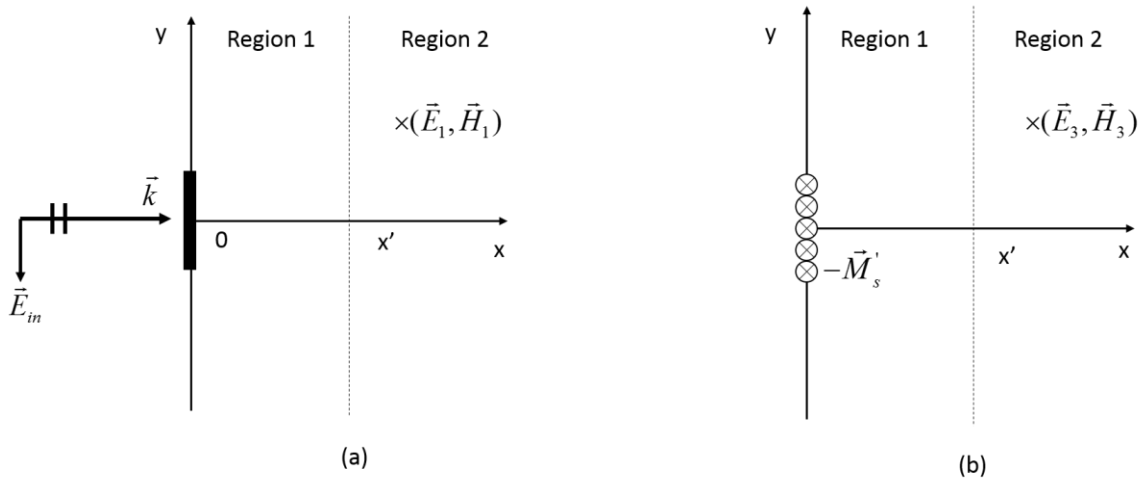


Figure 2.17: Modified equivalent problem of scattering for two plates (II)

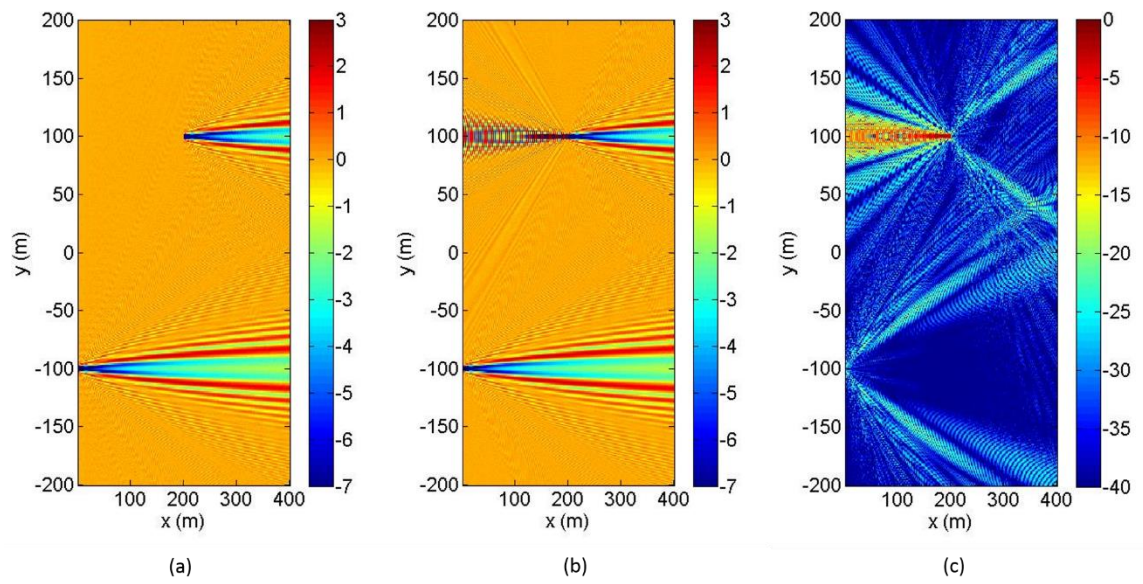


Figure 2.18: Amplitude of  $E_y$  component for two plates (TE). (a) Computed result by Huygens Principle. (b) Simulation result by FEKO. (c) Error

## TM CASE

For an incident plane wave of TM-polarization, the direction of equivalent magnetic current is along y-axis, as shown in Figure 2.19. In this model, the equivalent magnetic is infinitely long in z-axis and there is a gap between  $-a/2$  and  $+a/2$  along y-axis.

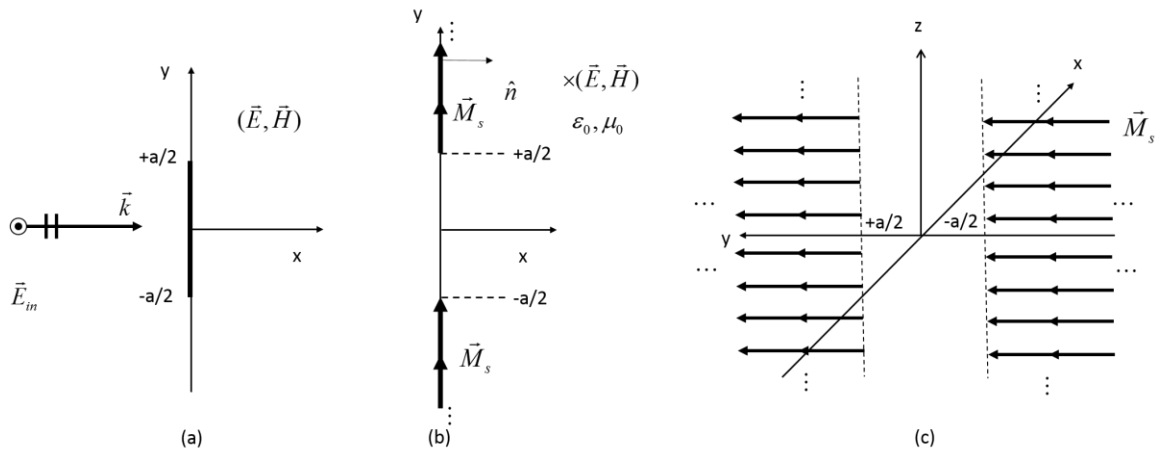


Figure 2.19: Equivalent problem for TM polarization. (a) Original Problem. (b)&(c) Equivalent problem

Since the equivalent magnetic current shown in Figure 2.19 is not z-directed, there should be an additional  $\sin \theta$  term for computing the field in this case as shown in Figure 2.20, compared to the one of TE-polarization case.

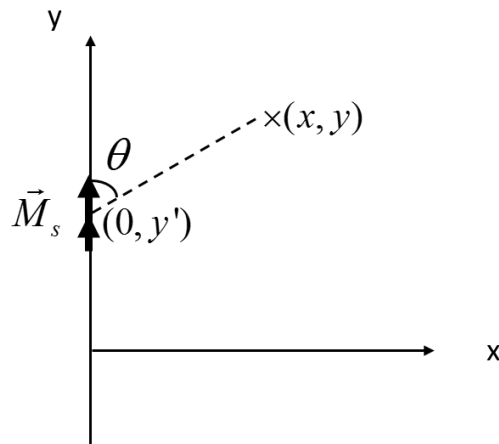


Figure 2.20: Radiation of a magnetic current directed along y-axis

Therefore the electric field at point (x,y) radiated by an infinitely long magnetic current  $I_m$  located at (0,y') can be estimated as

$$\begin{aligned}
 E_z &\approx I_m \sqrt{\frac{jk_0}{8\pi}} \frac{\exp(-jk_0 \sqrt{x^2 + (y-y')^2})}{\sqrt[4]{x^2 + (y-y')^2}} \sin \theta \\
 &= I_m \sqrt{\frac{jk_0}{8\pi}} \frac{\exp(-jk_0 \sqrt{x^2 + (y-y')^2})}{(x^2 + (y-y')^2)^{\frac{3}{4}}} x
 \end{aligned} \tag{2-40}$$

Using same approximations in TE case, the electric field at (x,y) can be expressed as

$$\begin{aligned}
 E_z(x, y) &= +2\sqrt{\frac{jk_0}{8\pi}} \left( \int_{-\infty}^{-\frac{a}{2}} \frac{\exp(-jk_0(x + \frac{1}{2x}(y-y')^2))}{\sqrt{x}} dy' + \int_{+\frac{a}{2}}^{+\infty} \frac{\exp(-jk_0(x + \frac{1}{2x}(y-y')^2))}{\sqrt{x}} dy' \right) \\
 &= +2\sqrt{\frac{jk_0}{8\pi}} \frac{\exp(-jk_0(x + \frac{y^2}{2x}))}{\sqrt{x}} \left( \int_{-\infty}^{-\frac{a}{2}} \exp(-Ay'^2 + By') dy' + \int_{+\frac{a}{2}}^{+\infty} \exp(-Ay'^2 + By') dy' \right)
 \end{aligned} \tag{2-41}$$

where  $A = \frac{jk_0}{2x}$ ,  $B = \frac{jk_0 y}{x}$ . It can be shown that this solution is same to the  $E_y$

component of TE case except here the sign is positive.

### TM COMPUTED RESULTS

Figure 2.21 shows the computed results of the computation and the corresponding error. Compared with the TE case, for the region close to x=0 the error is larger in TM polarization, due to the approximation made previously.

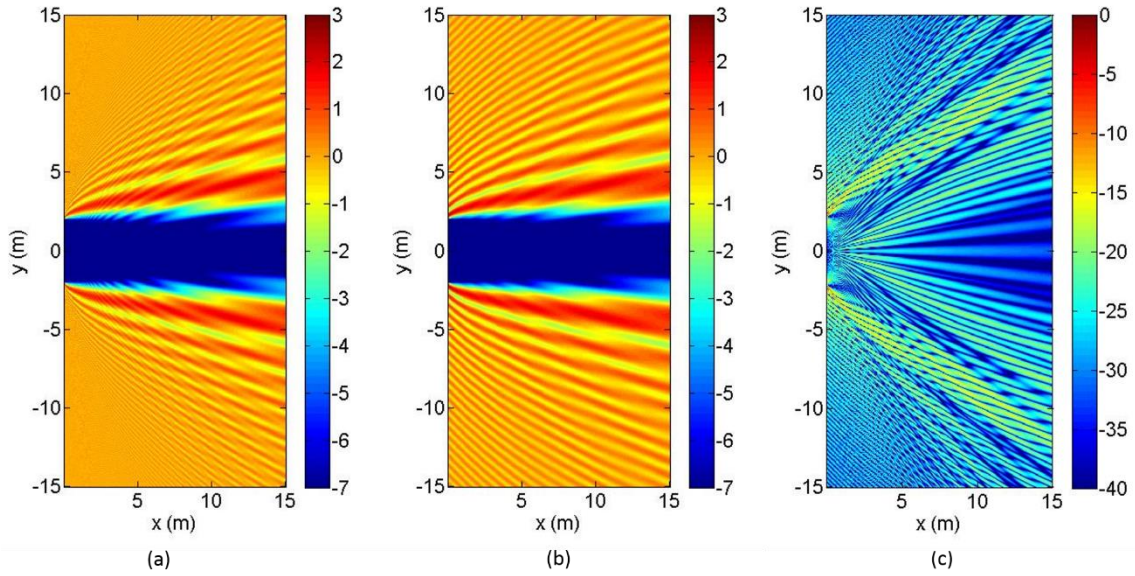


Figure 2.21: Amplitude of  $E_z$  component for TM polarization. (a) Computed result by Huygens Principle. (b) Simulation result by FEKO. (c) Relative error

### MODIFIED EQUIVALENT PROBLEM FOR TM

For TM case, we can also utilize the modified equivalent problem as shown in Figure 2.22, where the field we want to compute is  $\vec{E} = \vec{E}_1 + \vec{E}_2$ .  $\vec{E}_1$  is equal to the incident field while  $\vec{E}_2$  is radiated by the surface magnetic current shown in Figure 2.23. Figure 2.24 shows the computed result, which is equal to the one of Figure 2.20(a).

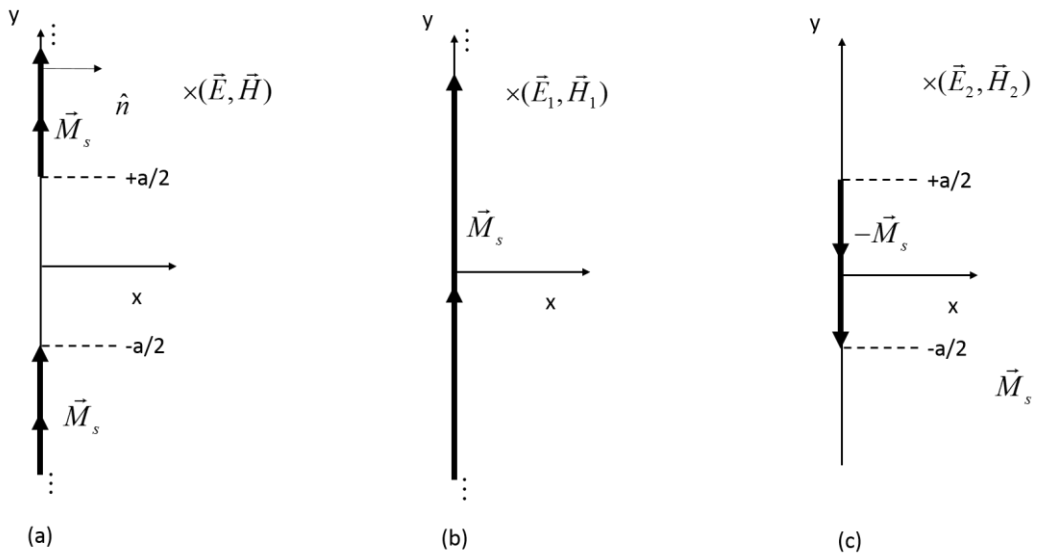


Figure 2.22: Modified equivalent problem for TE. (a) Original equivalent problem. (b)&(c) Modified equivalent problem

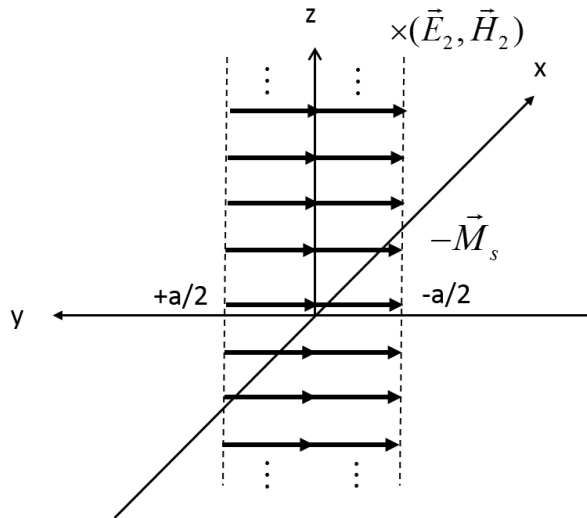


Figure 2.23: Radiation of a surface magnetic current oriented to  $y$ -direction

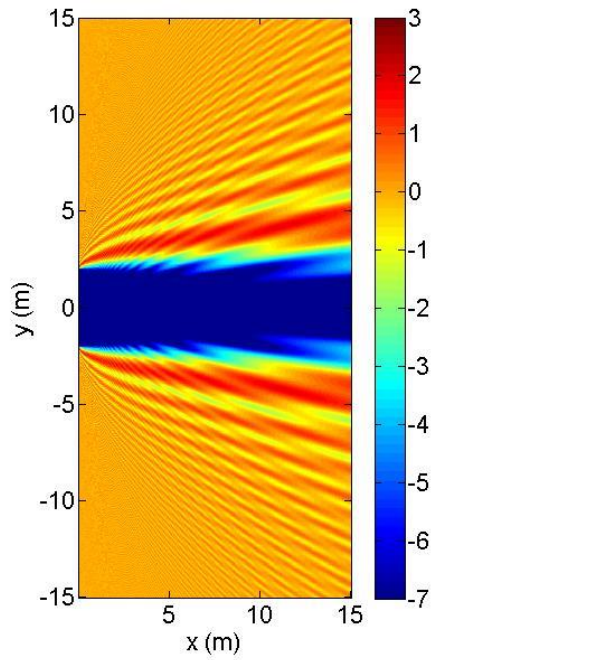


Figure 2.24: Computed results for modified equivalent problem of TM polarization.

### **BACKWARD PROPAGATION REGION**

For the backward propagation region, we can still use Huygens Principle to construct an equivalent problem, as shown in Figure 2.25 (for TM case as example). Since the plate model is not a good approximation of the original cylinder problem for the backward propagation region, we will not discuss it in detail.

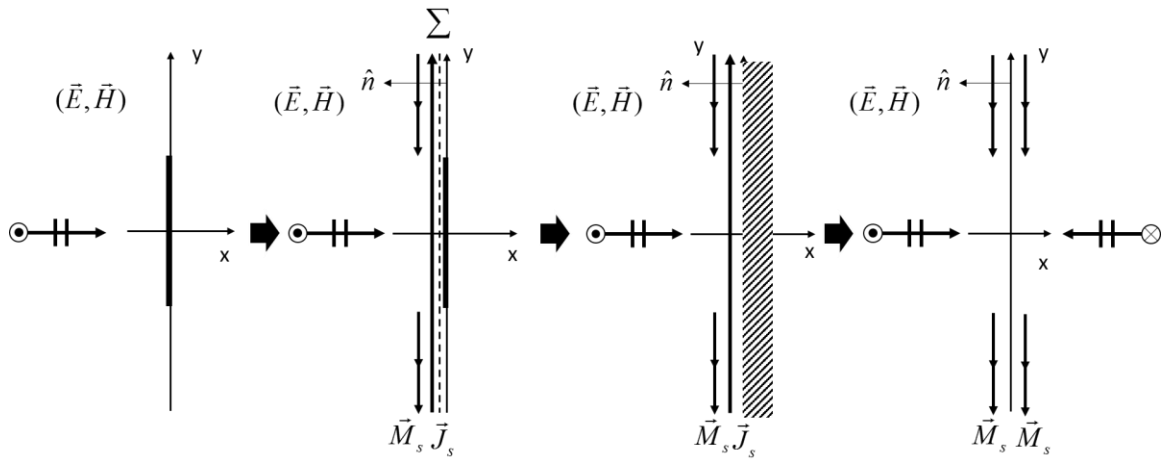


Figure 2.25: Construction of equivalent problem for backward propagation region using Huygens Principle

#### COMPARISON WITH CYLINDER MODEL

Figure 2.26 shows the comparison between the computation for a plate model using Huygens Principle and the simulation of a cylinder model using FEKO, both under TM polarization incidence at 500MHz. The result is reasonable in the shadow region (less than -16dB), although it is not satisfactory at large propagation angle (larger than -10dB), which is due to the simplified model and far-field approximation used here. Thus, using the plate model solved by Huygens Principle can give a reference result in studying the shadow region of the wind turbine farm. In Chapter 3, we will use a different approach to try to get a better solution.

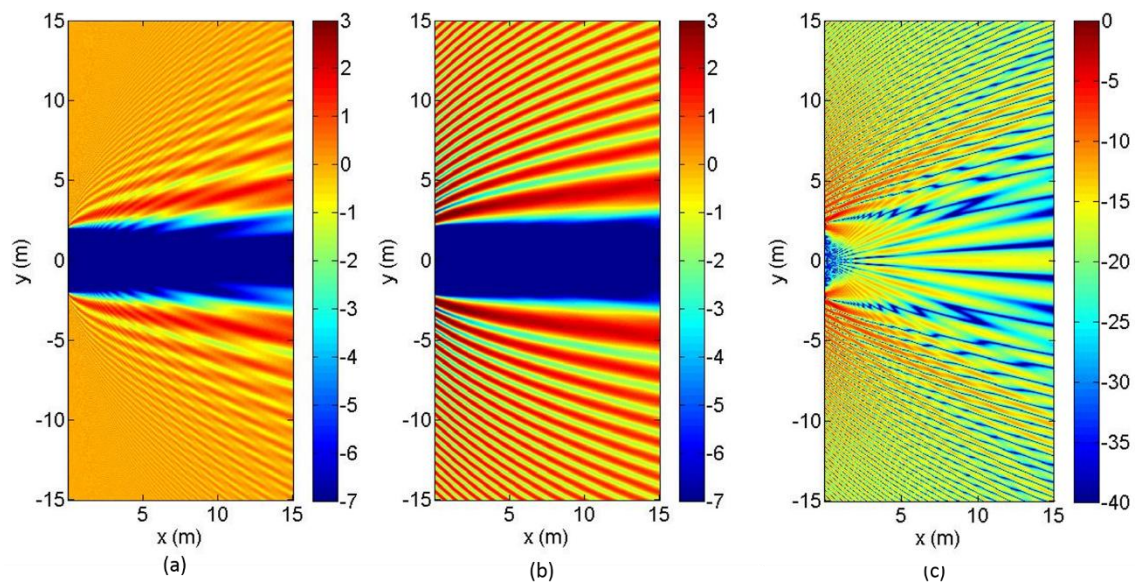


Figure 2.26: Comparison between plate model and cylinder model. (a) Computation of plate model using Huygens Principle. (b) Simulation of cylinder model using FEKO. (c) Relative error between (a) and (b)

## Chapter 3: Parabolic Equation Solution

In Chapter 2, it is shown that Huygens Principle with the error function can provide a good computed result for the plate model. However, for the cylinder model which is much closer to the original wind turbine problem, other methods are needed for more accurate results. In this chapter, a parabolic equation approach is implemented to solve the two-dimensional scattering problem of the cylinder model.

### INTRODUCTION AND DERIVATION

The parabolic equation (PE) is an approximation of the wave equation which models power propagating in a cone centered on a preferred direction – the paraxial direction. It was introduced by Leontovich and Fock in the 1940s [25] and has been extensively used in wave propagation modelling since the 1980s.

First, this method starts with assuming  $\exp(j\omega t)$  time-dependence of the fields, where  $\omega$  is the angular frequency. As shown in last section, we are only concerned with a two-dimensional problem where the field is independent of coordinate  $z$ . We define the field component we are interested as  $\psi$  which is only a function of  $x$  and  $y$ . For TM polarization,

$$\psi(x, y) = E_z(x, y) \quad (3-1)$$

while for TE polarization,

$$\psi(x, y) = H_z(x, y) \quad (3-2)$$

The parabolic equation technique is derived for solving problems where power propagates predominantly in the paraxial direction. We select the positive  $x$ -direction as the paraxial direction, as shown in Figure 3.1.

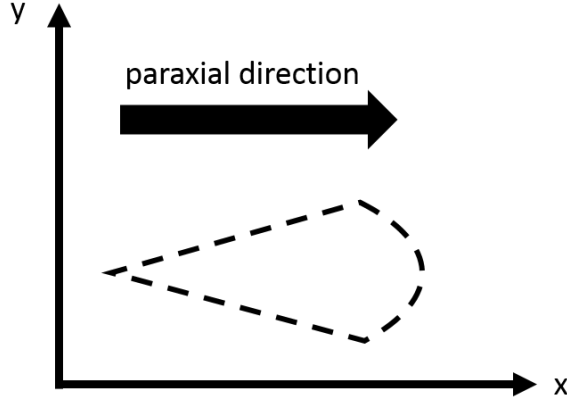


Figure 3.1: The propagation directions constitute the paraxial zone

For a homogeneous medium without any sources,  $\psi$  satisfies the two-dimensional scalar wave equation

$$\frac{\partial^2 \psi}{\partial x^2} + \frac{\partial^2 \psi}{\partial y^2} + k_0^2 n^2 \psi = 0 \quad (3-3)$$

where  $n$  is the refractive index and  $k_0$  is the wave number in free space. The reduced function is introduced associated with the paraxial direction  $+x$

$$u(x, y) = e^{+jk_0 x} \psi(x, y) \quad (3-4)$$

The reduced function is used because it is slowly varying in range for power propagating at angles close to the paraxial direction, giving it convenient numerical properties [26].

Then the scalar wave equation in terms of  $u$  is

$$\frac{\partial^2 u}{\partial x^2} - 2jk_0 \frac{\partial u}{\partial x} + \frac{\partial^2 u}{\partial y^2} + k_0^2 (n^2 - 1)u = 0 \quad (3-5)$$

which can be factored as

$$\left(\frac{\partial}{\partial x} - jk_0(1 - \sqrt{Q})\right)\left(\frac{\partial}{\partial x} - jk_0(1 + \sqrt{Q})\right)u = 0 \quad (3-6)$$

where  $Q$  is a pseudo-differential operator which is defined as

$$Q = \frac{1}{k_0^2} \frac{\partial^2}{\partial y^2} + n^2 \quad (3-7)$$

We can split the wave equation into two terms which respectively correspond to forward and backward propagating waves

$$\frac{\partial u}{\partial x} = jk_0(1 - \sqrt{Q})u \quad (3-8)$$

$$\frac{\partial u}{\partial x} = jk_0(1 + \sqrt{Q})u \quad (3-9)$$

in which the forward propagation corresponds to a wave propagating along the positive x-direction (Eqn. 3-8) and the backward propagation corresponds to the ones along negative x-direction (Eqn. 3-9). However, a single solution to Eqn. 3-8 or 3-9 is not, in general, for the actual electromagnetic field since both of them neglect the wave component propagating along the other direction. In order to get the exact solution of the original wave equation, the equations above should be solved simultaneously in a coupled system

$$u = u_+ + u_- \quad (3-10)$$

$$\frac{\partial u_+}{\partial x} = jk_0(1 - \sqrt{Q})u_+ \quad (3-11)$$

$$\frac{\partial u_-}{\partial x} = jk_0(1 + \sqrt{Q})u_- \quad (3-12)$$

So we can solve for energy propagating in a paraxial cone centered on both the positive and negative x-direction separately and then sum them up to get the total field.

#### STANDARD PARABOLIC EQUATION

In order to solve Eqn. 3-8 or 3-9, we have to make an approximation for the square-root. A simple way is to utilize a Taylor expansion

$$\sqrt{Q} = \sqrt{1 + (Q-1)} = 1 + \frac{Q-1}{2} - \frac{(Q-1)^2}{8} + \sum_{n=3}^{\infty} (-1)^{n-1} \frac{(2n-3)!!}{2n!!} (Q-1)^n \quad (3-13)$$

Using the first-order expansion, Eqn. 3-8 yields the following equation

$$\frac{\partial^2 u}{\partial y^2} - 2jk_0 \frac{\partial u}{\partial x} + k_0^2(n^2 - 1)u = 0 \quad (3-14)$$

which is called the standard parabolic equation (SPE). The performance of the standard parabolic equation is limited to small propagation angles away from the paraxial direction. For a plane wave propagating at angle  $\alpha$  from the paraxial direction +x in free space ( $n=1$ ), the largest neglected term in Taylor expansion is  $\frac{(Q-1)^2}{8}u$  which is proportional to  $(\frac{1}{k_0^2}|\frac{\partial^2 u}{\partial y^2}|)^2$ . In free space, the reduced function of a plane wave can be expressed as

$$u = \exp(-jk_0 x \cos \alpha - jk_0 y \sin \alpha + jk_0 x) \quad (3-15)$$

Hence the error is proportional to  $\sin^4 \alpha$ , which goes from  $10^{-7}$  at an angle of  $1^\circ$  to  $10^{-3}$  at  $10^\circ$  and over  $10^{-2}$  at  $20^\circ$ . Therefore it is also called the  $15^\circ$ -approximation [27] since for angle larger than  $15^\circ$  the error is large. This shows that the standard parabolic equation is a narrow-angle approximation of the parabolic wave equation, whose accuracy is very good for long-range calculations. It can be solved numerically by either split-step Fourier techniques or finite-difference methods [26].

### WIDE-ANGLE SOLUTION

For problems involving large propagation angles, a more accurate approximation of the operator  $Q$  should be used. Higher order polynomial expansions cannot be utilized due to the instability in numerical schemes produced by it [28, 29]. One choice is to use the approach introduced by Claerbout [30]. The Claerbout solution involves a Padé-(1,1) approximation of the form

$$\sqrt{1+(Q-1)} \approx \frac{1+a(Q-1)}{1+b(Q-1)} \quad (3-16)$$

Since the Taylor expansion of the right side of Eqn. 3-16 is

$$\frac{1+a(Q-1)}{1+b(Q-1)} = 1 + (Q-1)(a-b) + b(Q-1)^2(b-a) + b^2(Q-1)^3(a-b) + \dots \quad (3-17)$$

it is found that when  $a=0.75$ ,  $b=0.25$ , both sides of Eqn. 3-16 have the same Taylor expansion of order 2

$$\frac{1+0.75(Q-1)}{1+0.25(Q-1)} = 1 + \frac{Q-1}{2} - \frac{(Q-1)^2}{8} + \dots \quad (3-18)$$

Using the Claerbout solution, Eqn. 3-8 yields the following equation

$$\left(1 + \frac{Q-1}{4}\right) \frac{\partial u}{\partial x} + jk_0 \frac{Q-1}{2} u = 0 \quad (3-19)$$

According to Eqn. 3-7 and 3-15,

$$\left| \left(1 + \frac{Q-1}{4}\right) \frac{\partial u}{\partial x} + jk_0 \frac{Q-1}{2} u \right| = 2k_0 \left(\sin \frac{\alpha}{2}\right)^6 \quad (3-20)$$

Therefore, the error of using Claerbout solution for a plane wave propagating at angle  $\alpha$  from the x-axis is on the order of  $\sin^6 \alpha$ , which is acceptable for  $\alpha$  up to 45 degrees. Therefore, this approximation is also called the 45°-approximation [27].

Finally, the wide-angle parabolic equation for forward propagation becomes

$$\frac{\partial^2 u}{\partial z^2} - 2jk_0 \frac{\partial u}{\partial x} - \frac{j}{2k_0} \frac{\partial^2}{\partial z^2} \left(\frac{\partial u}{\partial x}\right) = 0 \quad (3-21)$$

## FINITE-DIFFERENCE IMPLEMENTATION

The parabolic equation can be implemented by either the split-step Fourier technique or the finite-difference methods. Since the Fourier technique does not have the necessary flexibility for boundary modelling, especially for problems including different types of boundary conditions [26], we select the finite-difference implementations to solve the parabolic equation. The Crank-Nicolson finite-difference scheme we utilize here is shown in Figure 3.2, which permits the modelling of arbitrary boundaries.

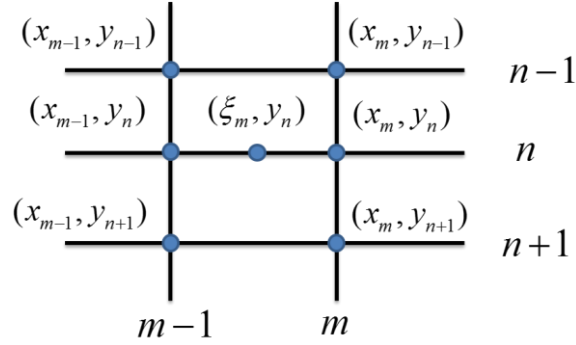


Figure 3.2: Crank-Nicolson finite-difference scheme ( $\xi_m = \frac{x_{m-1} + x_m}{2}$ ).

Using a central finite-difference approximation, the derivative along the x-axis and the second order derivative along the y-axis are respectively given by

$$\frac{\partial u}{\partial x}(\xi_m, y_n) \approx \frac{u(x_m, y_n) - u(x_{m-1}, y_n)}{\Delta x} \quad (3-22)$$

$$\frac{\partial^2 u}{\partial y^2}(\xi_m, y_n) \approx \frac{u(\xi_m, y_{n+1}) + u(\xi_m, y_{n-1}) - 2u(\xi_m, y_n)}{\Delta z^2} \quad (3-23)$$

where  $\Delta x = x_m - x_{m-1}$  and  $\Delta y = y_n - y_{n-1}$ . Using this approximation, Eqn. 3-21 yields the following update equation

$$u_n^m a + u_{n+1}^m b + u_{n-1}^m c = u_n^{m-1} d + u_{n+1}^{m-1} e + u_{n-1}^{m-1} f \quad (3-24)$$

where

$$\begin{aligned} a &= -\frac{1}{\Delta z^2} + \frac{2ik_0}{\Delta x} + \frac{j}{k_0 \Delta x \Delta z^2}, b = c = +\frac{1}{2\Delta z^2} - \frac{j}{2k_0 \Delta x \Delta z^2} \\ d &= +\frac{1}{\Delta z^2} + \frac{2ik_0}{\Delta x} + \frac{j}{k_0 \Delta x \Delta z^2}, e = f = -\frac{1}{2\Delta z^2} - \frac{j}{2k_0 \Delta x \Delta z^2} \end{aligned} \quad (3-25)$$

for  $m=1, 2, \dots, M-1$ . Here we have expressed the values at  $x_m$  as a function of values at  $x_{m-1}$  in the form of a linear system. In matrix form, we can rewrite Eqn. 3-24 in the following way

$$A_m U_m = V_m \quad (3-26)$$

where  $U_m$  is a column vector

$$U_m = \begin{pmatrix} u_0^m \\ \vdots \\ u_N^m \end{pmatrix} \quad (3-27)$$

$A_m$  is a tridiagonal matrix

$$A_m = \begin{pmatrix} 1 & 0 & 0 & 0 & 0 & \cdots & 0 & 0 & 0 & 0 \\ c & a & b & 0 & 0 & \cdots & 0 & 0 & 0 & 0 \\ 0 & c & a & b & 0 & \cdots & 0 & 0 & 0 & 0 \\ \vdots & \vdots & \vdots & \vdots & \vdots & & \vdots & \vdots & \vdots & \vdots \\ 0 & 0 & 0 & 0 & 0 & \cdots & 0 & c & a & b \\ 0 & 0 & 0 & 0 & 0 & \cdots & 0 & 0 & 0 & 1 \end{pmatrix} \quad (3-28)$$

and the right-hand side  $V_m$  is obtained from  $U_{m-1}$  by the matrix multiplication

$$V_m = \begin{pmatrix} 1 & 0 & 0 & 0 & 0 & \cdots & 0 & 0 & 0 & 0 \\ f & d & e & 0 & 0 & \cdots & 0 & 0 & 0 & 0 \\ 0 & f & d & e & 0 & \cdots & 0 & 0 & 0 & 0 \\ \vdots & \vdots & \vdots & \vdots & \vdots & & \vdots & \vdots & \vdots & \vdots \\ 0 & 0 & 0 & 0 & 0 & \cdots & 0 & f & d & e \\ 0 & 0 & 0 & 0 & 0 & \cdots & 0 & 0 & 0 & 1 \end{pmatrix} U_{m-1} \quad (3-29)$$

### INITIAL VERTICAL PLANE

The computation should start with the field on an initial vertical plane. For the forward propagation equation, we can select whichever vertical plane that is ahead of the scatterer since the total field propagating along the forward direction (positive x-axis here) is only the incident field. For a plane wave incident along the positive x-axis, we assume the incident field is

$$\psi(x, y) = \exp(-jk_0 x) \quad (3-30)$$

and its corresponding reduced function is

$$u(x, y) = \exp(jk_0 x)\psi(x, y) = 1 \quad (3-31)$$

Therefore we can assume that at the initial vertical plane  $x = x_0$ , the column vector  $U_0$

is

$$U_0 = \begin{pmatrix} 1 \\ 1 \\ \vdots \\ 1 \end{pmatrix} \quad (3-32)$$

We can then utilize the update equation to compute  $U_1, U_2 \dots U_{M-1}$ .

In the case above, we will compute the total field everywhere. We can also compute the scattered field instead. Therefore we can also start with the scattered field on an initial vertical plane ahead of the cylinder. In this region the scattered field propagating along positive x-direction is zero. Then the matrix  $U_0$  becomes

$$U_0 = \begin{pmatrix} 0 \\ 0 \\ \vdots \\ 0 \end{pmatrix} \quad (3-33)$$

### **BOUNDARY CONDITION (I)**

The difference between the process of computing the total field and scattered field is that we need to enforce different conditions inside the PEC cylinder. It is known that, inside the PEC, the total electric field is zero. So if we compute the total field, we need to enforce the following condition at every point (x,y) inside the cylinder,

$$u(x, y) = 0 \quad (3-34)$$

On the other hand, if we compute the scattered field, the condition to be enforced is

$$u^s(x, y) = -u^i(x, y) = -\exp(jk_0 x)\psi^i(x, y) = -1 \quad (3-35)$$

That means after computing the value of any column vector  $U_n$ , if there is a point (x,y) inside the cylinder, we need to enforce its value using Eqn. 3-34 or 3-35. For points along the boundary of the cylinder, the conditions is decided by the polarization of the incident wave. For the TM polarization,  $\psi$  is the transverse electric field  $E_z$  which must be zero on the boundary. Therefore the boundary condition can be still expressed as Eqn. 3-

34 or 3-35. For the TE polarization,  $\psi$  is the transverse magnetic field  $H_z$ , whose normal derivative is zero on the boundary

$$\frac{\partial \psi}{\partial \vec{n}} = 0 \quad (3-36)$$

where  $\vec{n}$  is the outer normal to the surface. It should be noted that the boundary conditions described here are not exact. This is because when enforcing the boundary conditions, we neglect the field propagating towards negative x direction, which is not exactly zero.

### BOUNDARY CONDITION (II)

In order to limit the integration domain in height, we need to enforce boundary conditions at the top and bottom boundary. They must be perfectly transparent, letting all power coming from below or above the boundary escape to infinity [26]. Here we choose the perfectly matched layer (PML) which is adequate for scattering applications. Assume the boundaries of the region we are interested in are respectively at  $y_{top}$  and  $y_{bot}$ . The PML is above  $y_{top}$  or below  $y_{bot}$ . We construct the two-dimensional PML by replacing the height  $y$  with complex coordinate  $\tilde{y}$  given by [31]

$$\tilde{y} = y - j \int_0^y \gamma(\zeta) d\zeta \quad (3-37)$$

where

$$\begin{cases} \gamma(z) = 0, & y_{bot} \leq y \leq y_{top} \\ \gamma(z) > 0, & y > y_{top} \text{ or } y < y_{bot} \end{cases}$$

Then we extend the wide-angle parabolic equation to the new coordinate

$$\frac{\partial^2 u}{\partial \tilde{y}^2} - 2jk_0 \frac{\partial u}{\partial x} - \frac{j}{2k_0} \frac{\partial^2}{\partial \tilde{y}^2} \frac{\partial u}{\partial x} = 0 \quad (3-38)$$

The solution of Eqn. 3-38 coincides with the usual parabolic solution for  $y_{bot} \leq y \leq y_{top}$  and has the form of a damped wave for  $y > y_{top}$  or  $y < y_{bot}$ . In order to implement the

PML with finite-difference, we rewrite the Eqn. 3-38 as

$$\frac{1}{1-j\sigma(y)} \frac{\partial}{\partial y} \left( \frac{1}{1-j\sigma(y)} \frac{\partial u}{\partial y} \right) - 2jk_0 \frac{\partial u}{\partial x} - \frac{j}{2k_0} \left( \frac{1}{1-j\sigma(y)} \frac{\partial}{\partial y} \left( \frac{1}{1-j\sigma(y)} \frac{\partial}{\partial y} \left( \frac{\partial u}{\partial x} \right) \right) \right) = 0 \quad (3-39)$$

where

$$\sigma(y) = \begin{cases} \sigma_0 \left( \frac{y - y_{top}}{\delta} \right)^2 & \text{for } y > y_{top} \\ 0 & \text{for } y_{bot} < y < y_{top} \\ \sigma_0 \left( \frac{y_{bot} - y}{\delta} \right)^2 & \text{for } y < y_{bot} \end{cases} \quad (3-40)$$

$$\sigma_0 = -\frac{3 \ln |R|}{2\delta} \quad (3-41)$$

R is a small number and  $\delta$  is the thickness of the one-side PML. Then the update equation for the parabolic equation including the PML is

$$u_n^m a_n + u_{n+1}^m b_n + u_{n-1}^m c_n = u_n^{m-1} d_n + u_{n+1}^{m-1} e_n + u_{n-1}^{m-1} f_n \quad (3-42)$$

where

$$\begin{aligned} a_n &= -\frac{1}{(1-j\sigma(y_n))^2 \Delta y^2} - \frac{2jk_0}{\Delta x} + \frac{j}{k_0(1-j\sigma(y_n))^2 \Delta y^2 \Delta x} \\ b_n &= +\frac{j\sigma_0 y_n'}{2\Delta y \delta^2 (1-j\sigma(y_n))^3} + \frac{1}{2(1-j\sigma(y_n))^2 \Delta y^2} + \frac{\sigma_0 y_n'}{2k_0 \delta^2 \Delta y \Delta x (1-j\sigma(y_n))^3} - \frac{j}{2k_0(1-j\sigma(y_n))^2 \Delta y^2 \Delta x} \\ c_n &= -\frac{j\sigma_0 y_n'}{2\Delta y \delta^2 (1-j\sigma(y_n))^3} + \frac{1}{2(1-j\sigma(y_n))^2 \Delta y^2} - \frac{\sigma_0 y_n'}{2k_0 \delta^2 \Delta y \Delta x (1-j\sigma(y_n))^3} - \frac{j}{2k_0(1-j\sigma(y_n))^2 \Delta y^2 \Delta x} \\ d_n &= +\frac{1}{(1-j\sigma(y_n))^2 \Delta y^2} - \frac{2jk_0}{\Delta x} + \frac{j}{k_0(1-j\sigma(y_n))^2 \Delta y^2 \Delta x} \\ e_n &= -\frac{j\sigma_0 y_n'}{2\Delta y \delta^2 (1-j\sigma(y_n))^3} - \frac{1}{2(1-j\sigma(y_n))^2 \Delta y^2} + \frac{\sigma_0 y_n'}{2k_0 \delta^2 \Delta y \Delta x (1-j\sigma(y_n))^3} - \frac{j}{2k_0(1-j\sigma(y_n))^2 \Delta y^2 \Delta x} \\ f_n &= +\frac{j\sigma_0 y_n'}{2\Delta y \delta^2 (1-j\sigma(y_n))^3} - \frac{1}{2(1-j\sigma(y_n))^2 \Delta y^2} - \frac{\sigma_0 y_n'}{2k_0 \delta^2 \Delta y \Delta x (1-j\sigma(y_n))^3} - \frac{j}{2k_0(1-j\sigma(y_n))^2 \Delta y^2 \Delta x} \end{aligned} \quad (3-43)$$

and

$$y' = \begin{cases} y - y_{top} & \text{for } y > y_{top} \\ 0 & \text{for } y_{bot} < y < y_{top} \\ y_{bot} - y & \text{for } y < y_{bot} \end{cases} \quad (3-44)$$

It can be found that for  $y'$  equal to zero, the update equation is the same as the one without PML (Eqn. 3-25).

## COMPUTED RESULTS OF FORWARD PROPAGATION

Assume there is an infinitely long PEC cylinder located at  $(0,0)$  with a diameter of 4 meters. The incident wave is TM-polarized and the amplitude of electric field is 1 V/m. The frequency is 500 MHz and the wavelength  $\lambda$  is 0.6 meters. Figure 3.3 shows the computed results by the parabolic equation with different sizes of mesh grid (assume  $\Delta x = \Delta y$  here). It should be noted that the computation starts from the region ahead of the cylinder, which is not shown in the results.

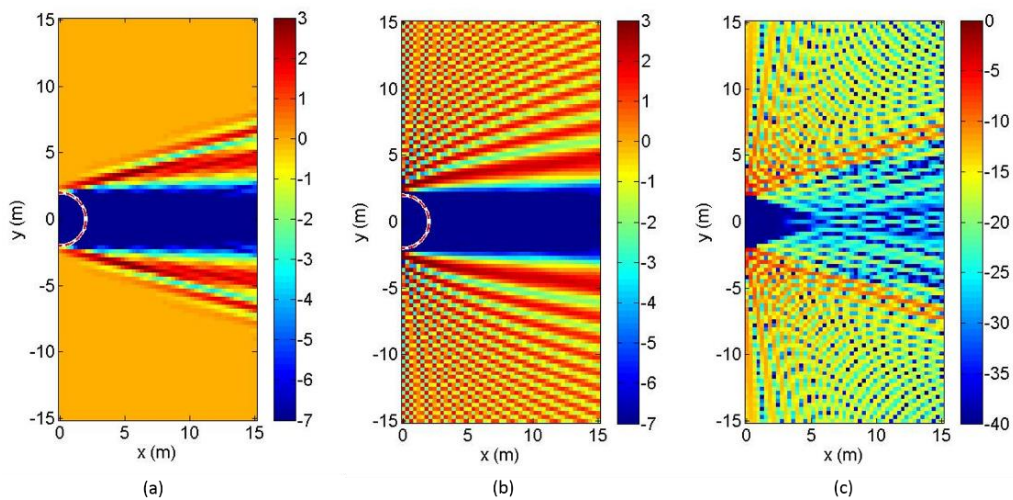


Figure 3.3: Computed result at mesh size equal to  $0.5 \lambda$ . (a) parabolic equation. (b) FEKO simulation. (c) Error

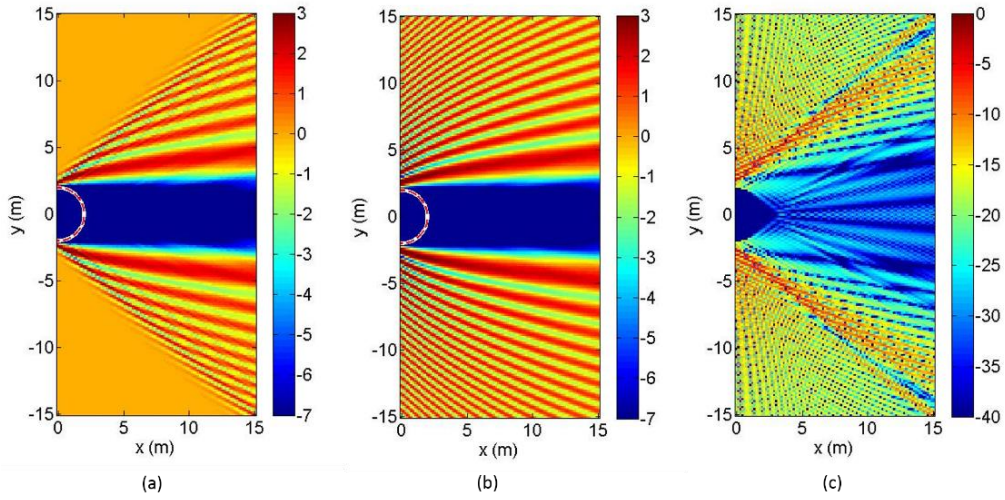


Figure 3.4: Computed result at mesh size equal to  $0.25 \lambda$ . (a) parabolic equation. (b) FEKO simulation. (c) Error

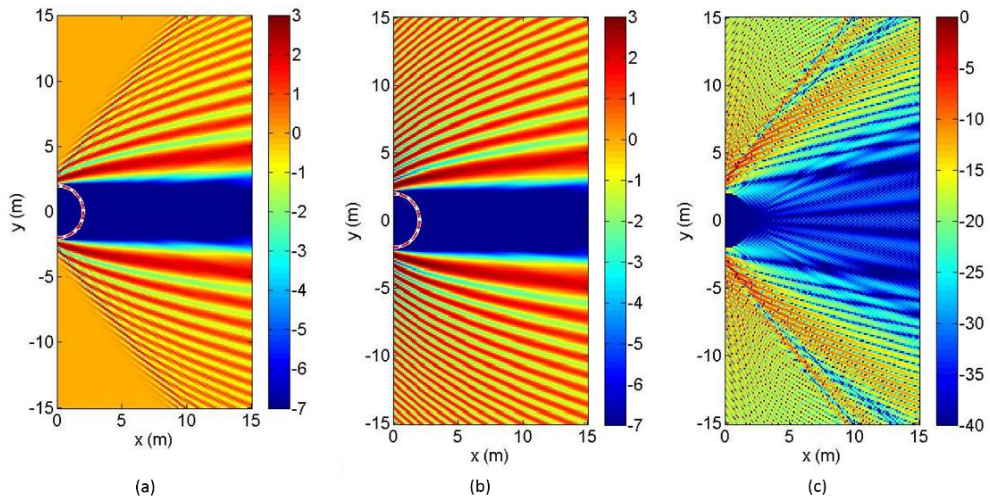


Figure 3.5: Computed result at mesh size equal to  $0.2 \lambda$ . (a) parabolic equation. (b) FEKO simulation. (c) Error

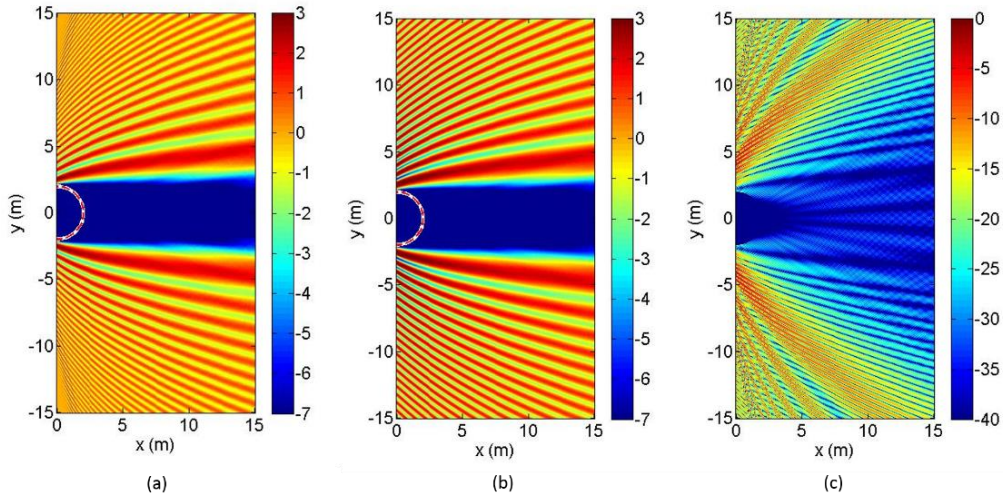


Figure 3.6: Computed result at mesh size equal to  $0.1 \lambda$ . (a) parabolic equation. (b) FEKO simulation. (c) Error

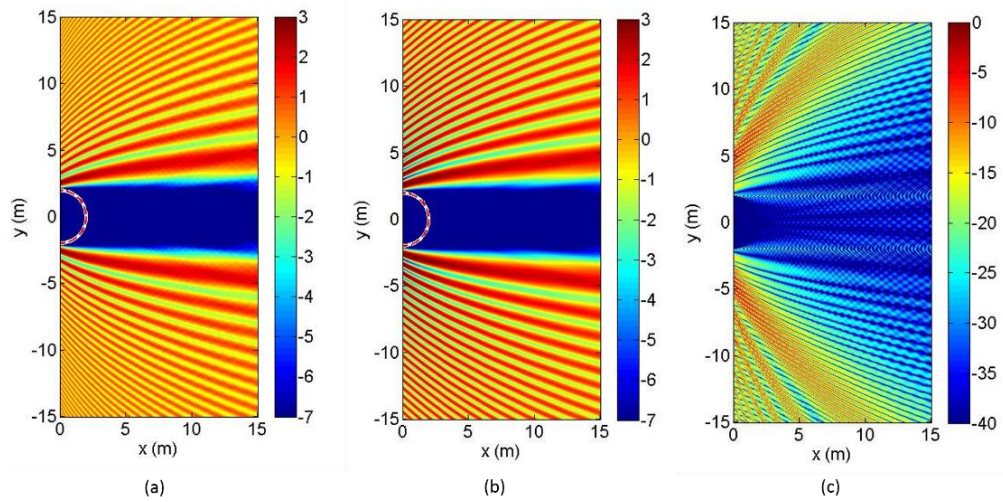


Figure 3.7: Computed result at mesh size equal to  $0.05 \lambda$ . (a) parabolic equation. (b) FEKO simulation. (c) Error

As shown in Figures 3.3(a), 3.4(a) and 3.5(a), when the mesh size is large, the interference between the incident field and scatter field cannot be found at large propagation angles. As the mesh size is further reduced, the interference pattern is

captured even at large propagation angles. From Figures 3.6(c) and 3.7(c), it is shown that the largest angle up to which the error is acceptable is about 45 degrees. This is due to the wide-angle approximation of operator Q we used here. In order to investigate the error further, here we define the percentage RMS error as

$$\%RMS\ error = \sqrt{\frac{\sum \| |E_{com}| - |E_{sim}| \|^2}{\sum |E_{sim}|^2}} \quad (3-45)$$

where  $E_{com}$  is the computed result by the parabolic equation while  $E_{sim}$  is the simulation result from FEKO. The %RMS error is integrated over the triangular region shown in Figure 3.8(a), where the propagation angle  $\alpha \in (-45^\circ, +45^\circ)$ , since the method used here cannot obtain the accurate results outside this region. The %RMS errors for different mesh sizes are plotted in Figure 3.8(b), with the numerical values shown in Table 3.1. Although the %RMS error does not converge at the mesh size equal to  $0.1\lambda$ , we can find that by this mesh size, the error in the shadow region is less than -30dB. Thus, if we are more interested in the field strength in the shadow region,  $0.1\lambda$  is suitable.

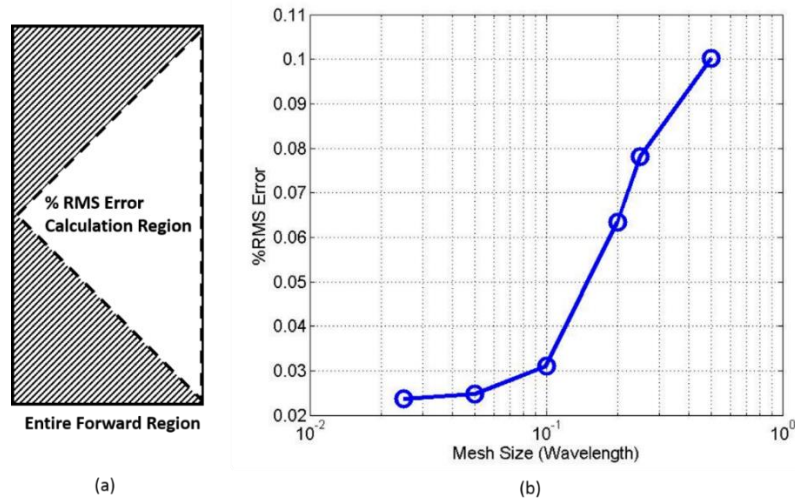


Figure 3.8: %RMS error with different mesh size. (a) Calculation region. (b) %RMS error.

Mesh Size (Wavelength)	%RMS Error
0.5	10.02%
0.25	7.81%
0.2	6.33%
0.1	3.11%
0.05	2.47%
0.025	2.36%

Table 3.1: %RMS with different mesh size

### BACKWARD PROPAGATION

For backward propagation equation, we can still use the Claerbout Approximation, then Eqn. 3-9 yields

$$\frac{\partial^2 u}{\partial y^2} + jk_0 \frac{\partial u}{\partial x} + \frac{j}{4k_0} \frac{\partial^2}{\partial y^2} \frac{\partial u}{\partial x} + 2k_0^2 u = 0 \quad (3-46)$$

Considering the PML, it becomes

$$\frac{1}{1-j\sigma(y)} \frac{\partial}{\partial y} \left( \frac{1}{1-j\sigma(y)} \frac{\partial u}{\partial y} \right) + jk_0 \frac{\partial u}{\partial x} + \frac{j}{4k_0} \left( \frac{1}{1-j\sigma(y)} \frac{\partial}{\partial y} \left( \frac{1}{1-j\sigma(y)} \frac{\partial}{\partial y} \left( \frac{\partial u}{\partial x} \right) \right) \right) + 2k_0^2 u = 0 \quad (3-47)$$

and the parameters for the update equation become

$$\begin{aligned}
a_n &= -\frac{1}{(1-j\sigma(y_n))^2\Delta y^2} + \frac{jk_0}{\Delta x} - \frac{j}{2k_0(1-j\sigma(y_n))^2\Delta y^2\Delta x} + k_0^2 \\
b_n &= +\frac{j\sigma_0 y_n'}{2\Delta y\delta^2(1-j\sigma(y_n))^3} + \frac{1}{2(1-j\sigma(y_n))^2\Delta y^2} - \frac{\sigma_0 y_n'}{4k_0\delta^2\Delta y\Delta x(1-j\sigma(y_n))^3} + \frac{j}{4k_0(1-j\sigma(y_n))^2\Delta y^2\Delta x} \\
c_n &= -\frac{j\sigma_0 y_n'}{2\Delta y\delta^2(1-j\sigma(y_n))^3} + \frac{1}{2(1-j\sigma(y_n))^2\Delta y^2} + \frac{\sigma_0 y_n'}{4k_0\delta^2\Delta y\Delta x(1-j\sigma(y_n))^3} + \frac{j}{4k_0(1-j\sigma(y_n))^2\Delta y^2\Delta x} \\
d_n &= +\frac{1}{(1-j\sigma(y_n))^2\Delta y^2} + \frac{jk_0}{\Delta x} - \frac{j}{2k_0(1-j\sigma(y_n))^2\Delta y^2\Delta x} - k_0^2 \\
e_n &= -\frac{j\sigma_0 y_n'}{2\Delta y\delta^2(1-j\sigma(y_n))^3} - \frac{1}{2(1-j\sigma(y_n))^2\Delta y^2} - \frac{\sigma_0 y_n'}{4k_0\delta^2\Delta y\Delta x(1-j\sigma(y_n))^3} + \frac{j}{4k_0(1-j\sigma(y_n))^2\Delta y^2\Delta x} \\
f_n &= +\frac{j\sigma_0 y_n'}{2\Delta y\delta^2(1+i\sigma(y_n))^3} - \frac{1}{2(1-j\sigma(y_n))^2\Delta y^2} + \frac{\sigma_0 y_n'}{4k_0\delta^2\Delta y\Delta x(1-j\sigma(y_n))^3} + \frac{j}{4k_0(1-j\sigma(y_n))^2\Delta y^2\Delta x}
\end{aligned} \tag{3-48}$$

The backward propagating field is obtained with a separate run, marching in the negative x-direction. The object is treated as a sequence of reflecting facets which act as sources for the backward propagating field [32-34], as is shown in Figure 3.9. In this case, since the incident field propagates along the positive x-direction, we can only calculate the backward scattered field by using the backward equation. Thus, this simulation starts at a vertical plane beyond the scatterer with the initial field equal to zero. Boundary conditions on each facet are given by the appropriate polarization-dependent reflection coefficients [26]. Since the reflecting facet is PEC, under a TM-polarized incidence, the reflection coefficient is equal to -1. In this case, we can assume the backward-propagating scattered electric field along the reflecting facet is equal to  $-\vec{E}_{in}$  while at the rest part of the cylinder it is equal to zero. In contrast, recall the process of the forward propagation computation, the forward-propagating scattered electric field inside the cylinder is also equal to  $-\vec{E}_{in}$ , which makes the two results different.

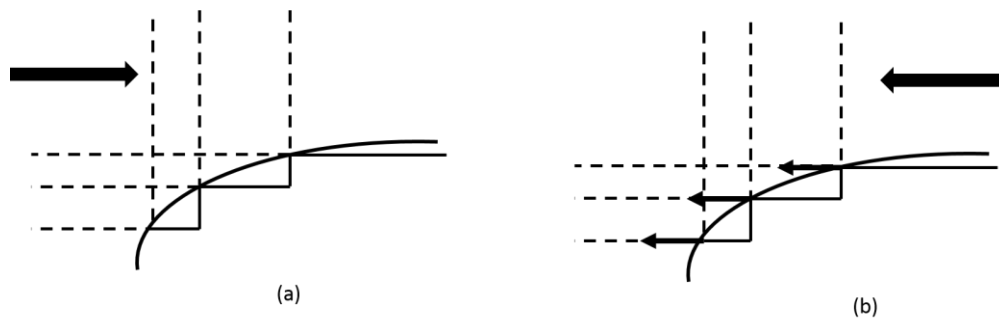


Figure 3.9: Facet Model. (a) Forward Propagation. (b) Backward Propagation.

### COMPUTED RESULTS OF BACKWARD PROPAGATION

Figure 3.10 shows the computed results for the backward propagation case, with a TM-polarized incident wave at 500MHz. It is found that larger mesh size cannot achieve acceptable results, so the mesh size here is  $0.01 \lambda$ . Due to the very small mesh size, the computation time is long. Also, the error outside the small propagation angle is somewhat significant. More suitable boundary conditions may need to be found.

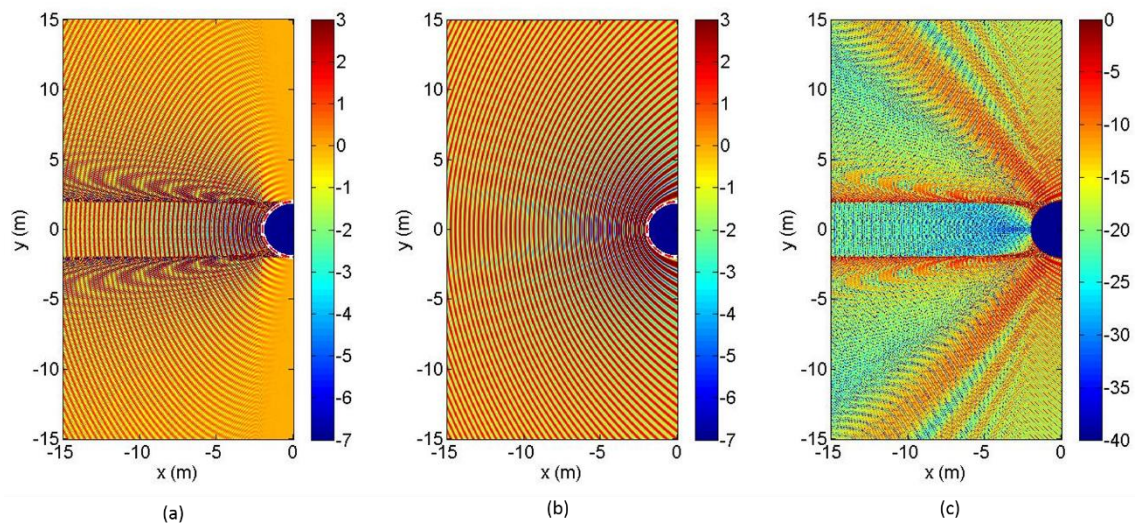


Figure 3.10: Computed result for backward propagation at mesh size equal to  $0.01 \lambda$ . (a) parabolic equation. (b) FEKO simulation. (c) Error

## COMPUTATION FOR MULTIPLE CYLINDERS

Consider the problem shown in Figure 3.11, which is a simplified model of a 3x3 wind farm. There are nine infinitely long PEC cylinders with same radius (2 meters). The coordinates of each cylinder is shown in Table 3.2. Using the parabolic equation technique, the computed results and corresponding comparison with FEKO simulation are shown in Figure 3.12. The error is mainly due to two factors: (1) the backward propagation which is not considered here and (2) the large angle propagation which always has error due to the approximation of pseudo-differential operator  $Q$ . For the region where the effect from these two factors is small, the error is about -20dB. Figure 3.13 shows the field distribution (in dB scale) behind some specific cylinders (No. 4, No. 7 and No. 9) along the red dash lines shown in Figure 3.11. It is shown that in the shadow region, both the computed results and the simulation results follow the same trend, except that in the simulation results the wave oscillation is much stronger. This error is mainly due to the backward scattering and wide-angle propagation which is not well solved in the parabolic equation solution. Since there is no backward scattering behind Cylinder No.9, the wave oscillation shown in Figure 3.13(c) is not as strong as the ones shown in Figure 3.13(a)&(b). However, there is some obvious offset shown in Figure 3.13(c), which is probably because that the error from both the backward scattering and wide-angle propagation is accumulated when the simulation is marching in the positive  $x$ -direction. As shown in both the computed results and the simulation results, Cylinder No.4 is not in the shadow region of any other cylinders, while Cylinder No. 7 is located in the shadow region of Cylinder No.2. Thus, in the shadow region of Cylinder No.7, the field fade is stronger than the Cylinder No.4. In the shadow region of Cylinder No.9, the fade is even stronger since it is in the shadow of both Cylinder No.1 and No.5.

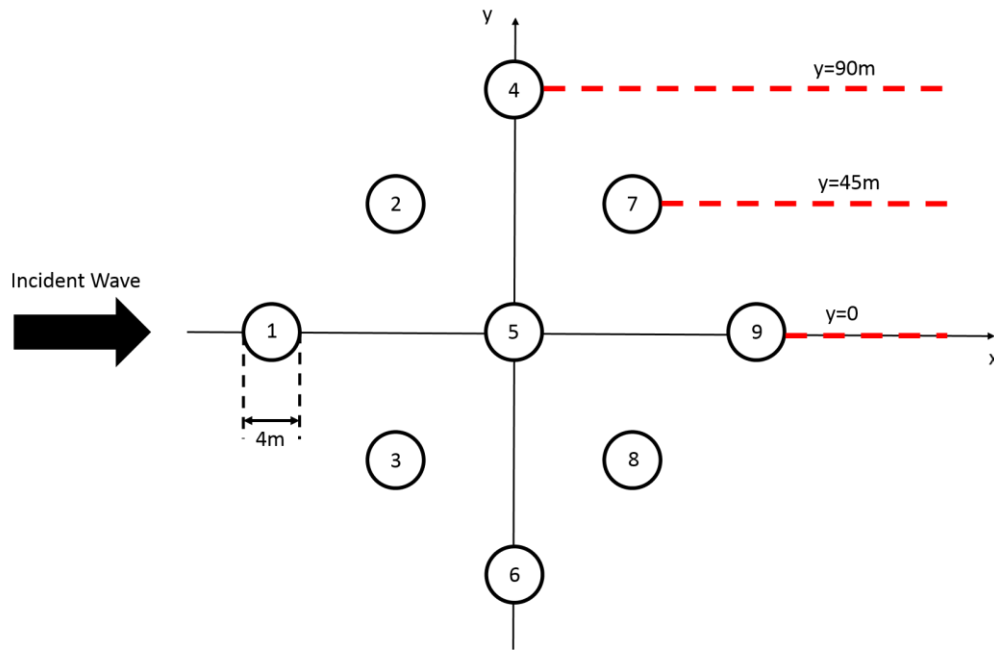


Figure 3.11: Simplified model of wind turbine farm

Number	Coordinates	Number	Coordinates
1	(-90,0)	6	(0,-90)
2	(-45,+45)	7	(+45,+45)
3	(-45,-45)	8	(+45,-45)
4	(0,+90)	9	(+90,0)
5	(0,0)		

Table 3.2: Coordinates of cylinders shown in Figure 3.11 (Unit:m)

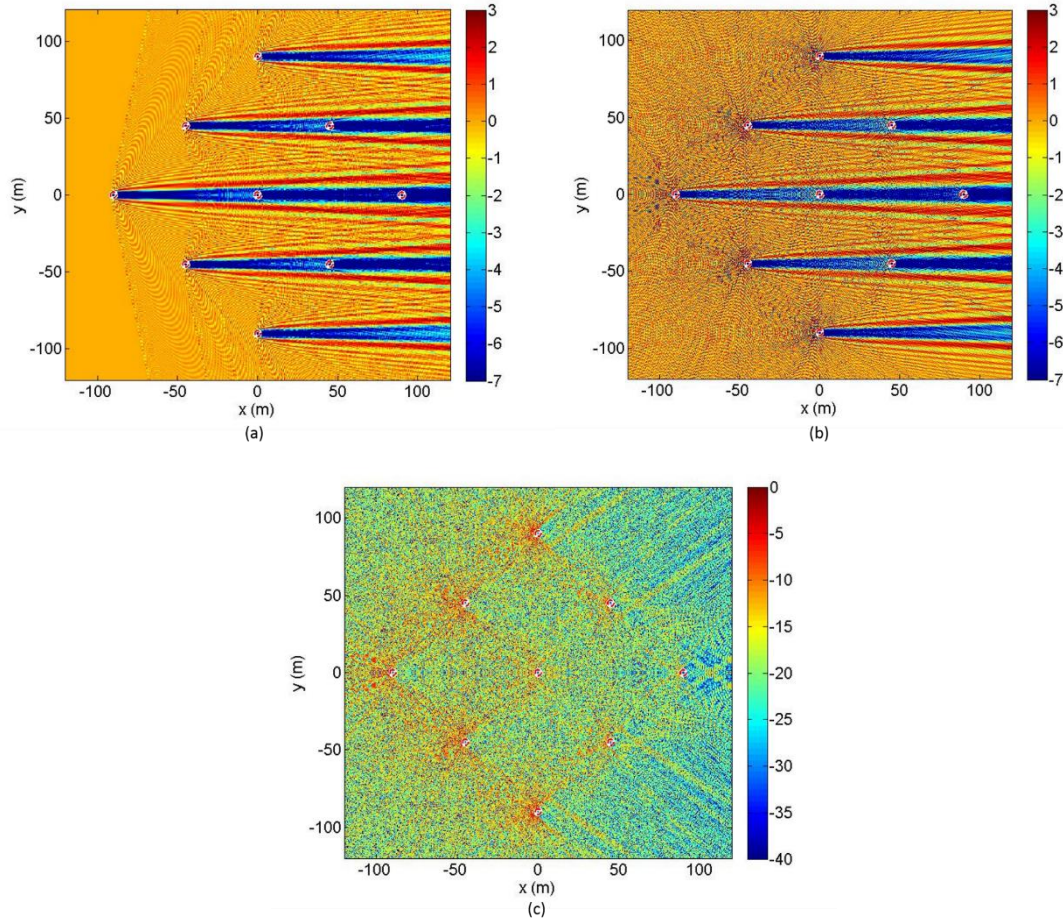


Figure 3.12: Scattering computation for a wind turbine farm. (a) parabolic equation solution. (b) FEKO simulation. (c) Error

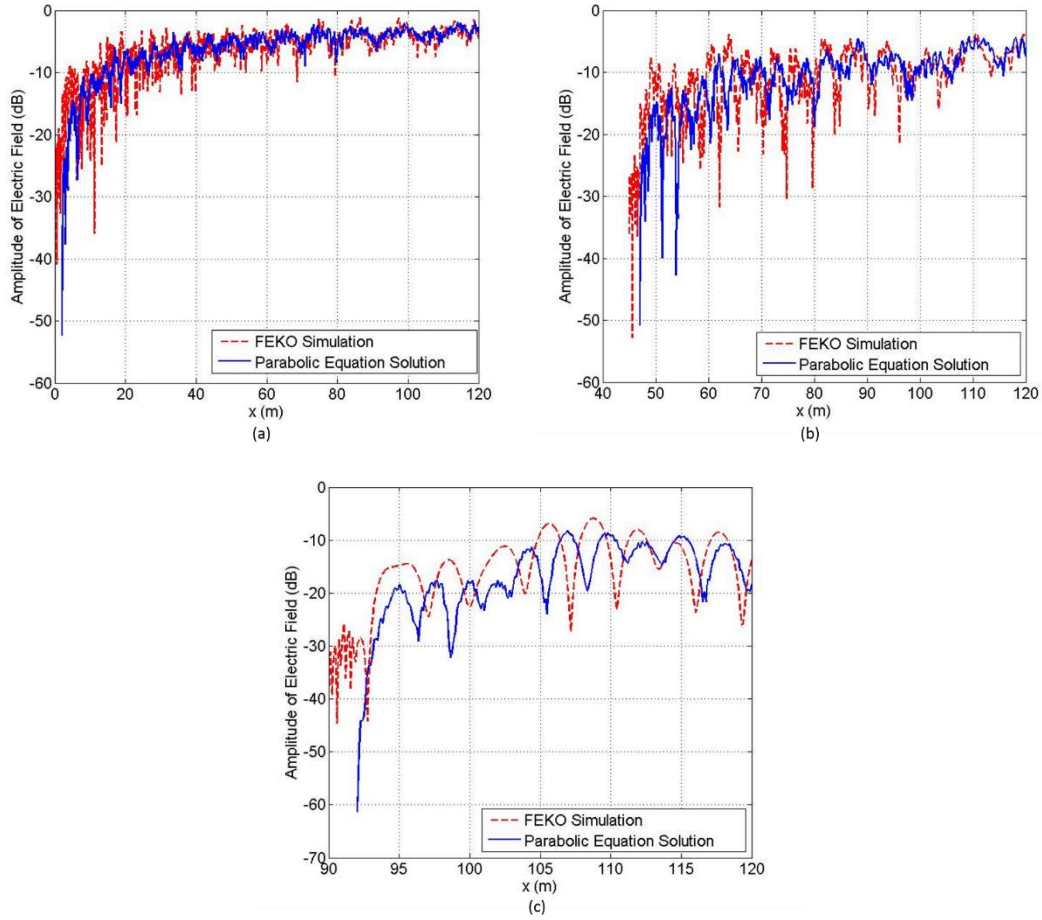


Figure 3.13: Field distribution behind specific cylinders. (a) Cylinder No.4. (b) Cylinder No.7. (c) Cylinder No.9.

### PARABOLIC EQUATION UNDER LINE SOURCE INCIDENCE

As will be shown in Chapter 4, we use two transceivers to measure the field distribution around a metal pole. However, we cannot use the transceiver to generate a plane wave incidence. Thus, the excitation in the parabolic equation has to be modified in order to be compare with the measurement results. Commonly, the transceiver should be regarded as a point source. However, we are solving a two-dimensional problem in this chapter, which is not suitable for a point source excitation. So we assume the source is an

infinite long current source along z-axis. Then the electric field radiated by it can be expressed as [24]

$$E_z = A \frac{\exp(-jk_0\rho)}{\sqrt{\rho}} \quad (3-49)$$

where  $A = -\eta_0 I_e \sqrt{\frac{jk_0}{8\pi}}$  is a constant decide by the amplitude of the source. Using this equation we can get the incident field  $\psi^{in}(x, y)$  everywhere. Since parabolic equation is most accurate for plane wave propagation, computing the total field due to a cylindrical incident wave here is not applicable. So here we use parabolic equation to compute the scatter field and enforce the conditions

$$u^s(x, y) = -u^{in}(x, y) = -\exp(jk_0x)\psi^{in}(x, y) \quad (3-50)$$

at the points inside the PEC cylinder. Using this approach, the field distribution around a PEC cylinder with a radius of 0.15m, under the excitation of an infinitely long current source located at (-1.2m, 0), with a frequency of 3.5GHz, is shown in Figure 3.14 (in dB scale). Here the backward propagation region is not considered since the measurement is only done in the forward propagation region.

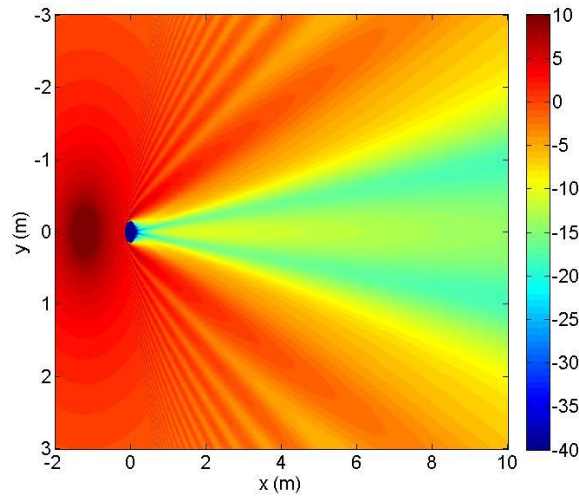


Figure 3.14: Field distribution under a line source incidence by parabolic equation

In this chapter, we used the parabolic equation technique to compute field distribution behind a PEC cylinder. The computed results are more accurate than the method of Huygens Principle used in Chapter 2, since here we solved the scattering problem of the cylinder model. In Chapter 4, we will do measurement using transceivers in order to further verify the results obtained in this chapter.

## Chapter 4: Measurement Using UWB Transceivers

In this chapter, two commercial ultra-wideband (UWB) transceivers from Time Domain Corporation (model P410) and the associated Channel Analysis Tool software are utilized to measure the field distribution around a metal pole. The measured results are then compared to the computed results by the parabolic equation approach. Fast Fourier transform is utilized to transform the time-domain results from the receiver into the frequency domain, since the parabolic equation solution is based in the frequency domain.

### TRANSCIVER AND CHANNEL ANALYSIS TOOL

We use two Time Domain P410 UWB transceivers (Figure 4.1) and their Channel Analysis Tool [35] to measure the electromagnetic field beyond a metal utility pole located at the University of Texas Pickle Research Campus. Each platform is connected to a broad band antenna that has an isotropic radiation pattern in the azimuth plane. One unit is set up as the receiver and it is placed in front of the pole. The other unit is set up as the transmitter, which is moved along various positions. The transmitter continuously sends very short RF pulses with an equivalent frequency bandwidth from 3.1 to 5.3 GHz and centered at 4.3 GHz. They propagate through the environment and is received and recorded by the receiver. By geometrical optics, we know that there are several path for wave to propagate between the transmitter and receiver. As shown in Figure 4.2, the direct path has the shortest delay time, which is recorded as the zero delay time point for each scan of the result generated by the Channel Analysis Tool, as shown in Figure 4.3. In Figure 4.3, the columns represent the delay time information relative to the direct path for each pulse sent by the transmitter. Due to the pole we want to measure, there is a multipath, like the “multipath 1” shown in Figure 4.2. Since the length of this multipath is

usually close to the direct path, its relative delay time is small. But due to the small length difference, the direct path and multipath interfere with each other constructively or destructively in the frequency domain when the transmitter is at different position, leading to spatial oscillations. There is also some other multipath due to other objects around, as shown as the “multipath 2” in Figure 4.2. Usually, the delay time is large, which can be found in the results shown in Figure 4.3. Due to the path loss, the field strength of multipath is lower than the direct path, which always has the largest amplitude.



Figure 4.1: Time Domain P410 UWB transceiver

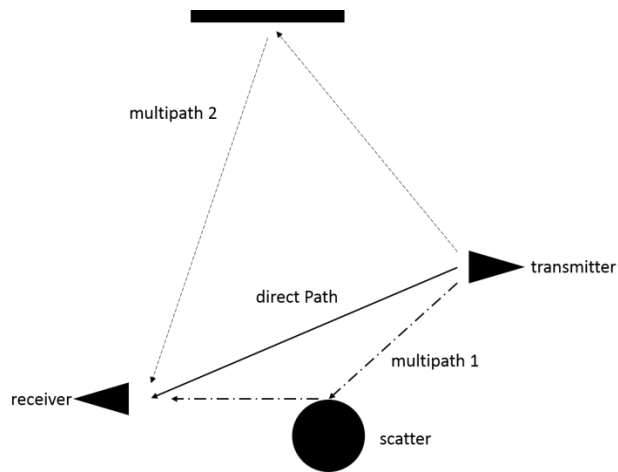


Figure 4.2: Direct path and multipath

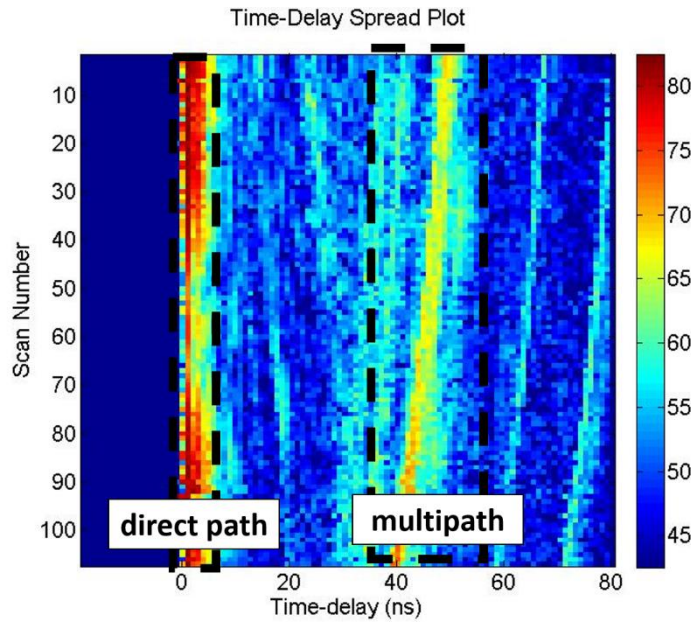


Figure 4.3: Measurement result by Channel Analysis Tool

**MEASUREMENT**

Since we need a laptop to record the data received by the receiver, it is more convenient to move the transmitter rather than the receiver (by reciprocity, the results are the same). We use the transceiver pair to measure the field strength behind a metal pole

with a radius of 0.15m at discrete locations, as shown in Figure 4.4. The transmitter is moved along the dashed line shown in Figure 4.5. If the transmitter is moved at a constant speed, the scan numbers can be directly mapped to position using a constant value.



Figure 4.4: Measurement Photos. (a) Metal pole to be measured. (b) Receiver.

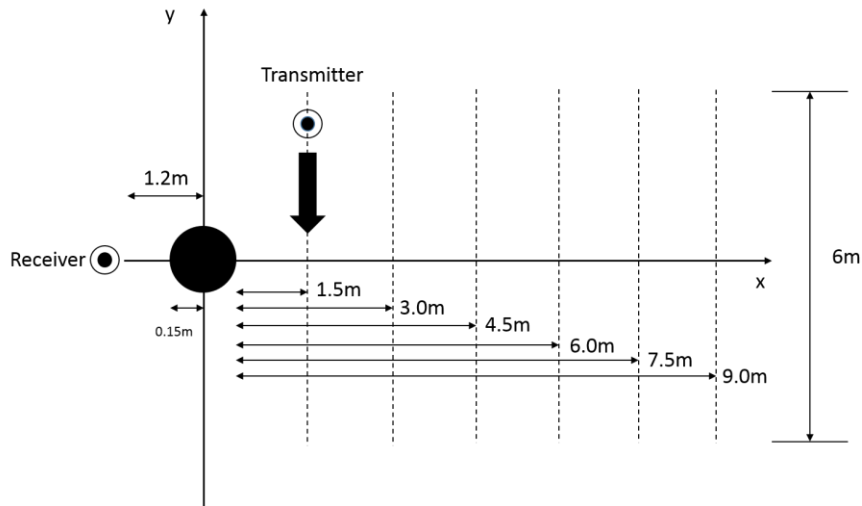


Figure 4.5: Scheme of measurement

## **DATA PROCESSING**

As is known, the results given by the Channel Analysis Tool is in the time domain. We need to transform it to the frequency domain by a fast Fourier transform. First, we need to eliminate the effect from multipath caused by other scatterers. Therefore, we only select the data close to the direct path. For example, for the result shown in Figure 4.3, we can choose the data between 0 and 20ns. Second, use a fast Fourier transform to process the data into the frequency domain and only record the data of the frequency we are interested in. The range sampling of the data in time is 61 ps which leads to a maximum frequency window of 16.4 GHz. Third, assuming the transmitter is moved at a constant speed, we can plot the field at different locations by directly mapping the scan numbers to position.

## **RESULTS COMPARISON**

The measurements were carried out twice for each vertical cut in Figure 4.5, and compared with the computed results from the parabolic equation approach. Due to the very close distance between the human body and the transmitter during measurement, there is a fading at the center frequency 4.3GHz. Thus, we choose the results of 3.5GHz, at which the measured field does not fade, instead of 4.3GHz. The results are summarized in Figure 4.6. It can be observed in both the computation and measurement that the shadow region appears in the center of the cuts and its width becomes larger when the observation cut is moved further away. Outside the shadow region, both the computed results and measurement results show the wave oscillation due to the multipath by the pole. Also, the field strength decays when the observation cut is farther away from the pole, which is due to the point source used here. For the results of the first four vertical cuts we measured, the computed field strength in the shadow region agrees well with the measurement (at most -2dB difference). In the region outside the shadow, at some

position the error is a little larger, which is probably due to the imperfect measurement we made. For the last two cuts, the error becomes larger (-5dB) in both the shadow region and outside region. The field strength of the measurement is lower than the computed results almost everywhere. One reason is that in the computation by the parabolic equation we solved a two-dimensional problem, which is quite different from the practical three-dimensional problem. The error may be also due to the multipath by the ground. It well-known that when the distance between the transmitter and receiver becomes large, the length of the multipath by the ground is very close to the direct path. Thus, the time delay of that multipath is quite small, which cannot be filtered from the measurement results in time domain. This multipath may lead to the decay of the field we measured.

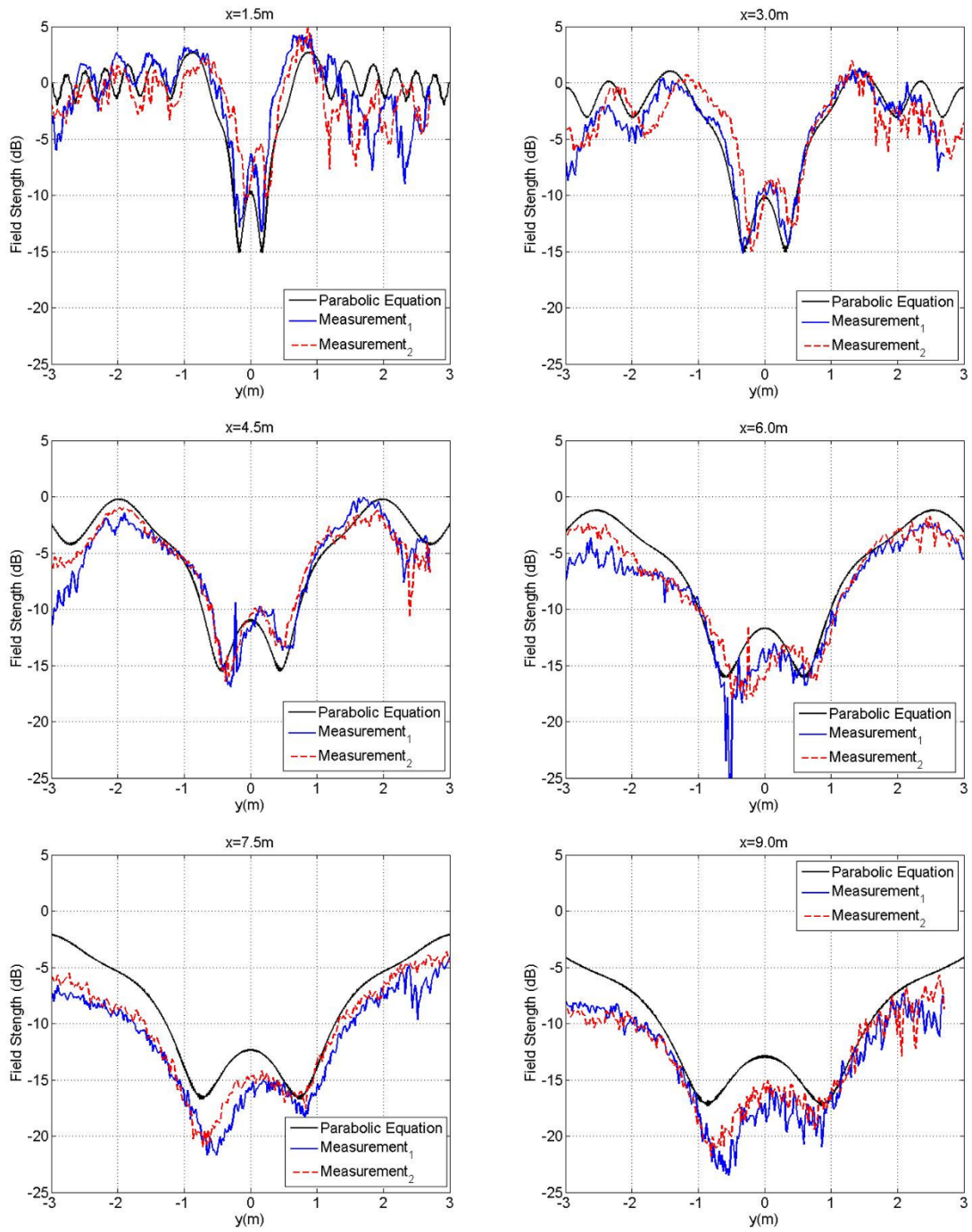


Figure 4.6: Comparison between computation and measurement for a metal pole

In this chapter, in order to verify the computed results from the parabolic equation, the near-field distribution of a metal pole was measured by using two transceivers. It was found that when the observation positions were close to the pole, the computed results agreed well with the measurement results. When the distance was large, the measured field strength was lower than the computed one, which was probably due to the multipath by the ground. Although the parabolic equation technique is not accurate for field at large propagation angles, it is useful for studying the shape and field strength of the wind turbine's shadow region.

## Chapter 5: Conclusion

In this thesis, two approaches for the scattering problem of wind turbine farm were investigated. Firstly, the cylinder model of the wind turbine was simplified further into the plate model. And the equivalent problem of this model was constructed by using Huygens Principle, which can be solved analytically by error function. TE and TM polarization was discussed respectively and the results were verified by FEKO simulation. As was shown in the results, although using this method can obtain the size of the shadow region, the field strength is not exact due to the different shape of the scatterer.

Secondly, parabolic equation technique was introduced and utilized to solve the problem for more accurate results. Wide-angle approximation and perfectly matching layers were selected and implemented by finite-difference method. The TM-polarized incidence case was discussed and solved. Due to the approximation it contains, the computed results at large propagation angle were not accurate. However, for small-angle propagation this method was applicable. It can compute both the size and field strength of the shadow region accurately.

Lastly, a measurement using Time Domain transceivers was designed. The measurement results along several parallel rows behind a metal pole were compared with the computed results by parabolic equation under a line source excitation. The results coincided well with each other, which showed that the parabolic equation is a good tool for solving the shadow problem of wind farms.

Some problems have also been identified for possible future work. The problem of backward propagation is not well solved in this thesis, which at present requires much smaller mesh size to obtain a result as accurate as the forward propagation case. Also, the

large angle problem for parabolic equation can be studied in the future, such as using the Split-step Padé method to solve the parabolic equation.

## References

- [1] Air Warfare Center, “The Effects of Wind Turbine Farms on ATC RADARS,” Air Warfare Center, Royal Air Force, London, UK, 2005.
- [2] C.A. Jackson, “Wind farm characteristics and their effect on radar systems,” in *Proceedings of International Conference on Radar Systems*, Edinburgh, October 2007.
- [3] J. J. Lemmon, J. E. Carroll, F. H. Sanders, and D. Turner, “Assessment of the effects of wind turbines on air traffic control radars,” National Telecommunications and Information Administration Technical Report 08-454, Department of Commerce, Boulder, CO, USA, 2008.
- [4] Air Warfare Center, “The Effects of Wind Turbine Farms on Air Defence Radars,” Royal Air Force, UK, Jan. 2005
- [5] Air Warfare Center, “Further Evidence of the Effects of Wind Turbine Farms on Air Defense RADARS,” Royal Air Force, UK, Aug. 2005.
- [6] R. J. Vogt, T. D. Crum, W. Greenwood, E. J. Ciardi, and R. G. Guenther, “New Criteria for Evaluating Wind Turbine Impacts on NEXRAD Weather Radars,” *WINDPOWER 2011*, Anaheim, CA, USA, 2011.
- [7] Air Warfare Center, “Further Evidence of the Effects of Wind Turbine Farms on Air Defense RADARS,” Royal Air Force, UK, Aug. 2005.
- [8] “The Effect of Windmills Farms on Military Readiness,” United States Department of Defense Report to the Congressional Defense Committees, 2006.
- [9] QinetiQ, “Results of the Electromagnetic Investigations and Assessments of Marine Radar, Communications and Positioning Systems Undertaken at the North Hoyle Wind Farm,” QinetiQ and the Maritime and Coastguard Agency, Salisbury, UK, 2004.

- [10] D. Vega, C. Frenandez, O. Grande, I Angulo, D. Guerra, Y. Wu, P. Angueira, and J. L. Ordiales, "Software tool for the analysis of potential impact of wind farms on radiocommunication services," in *IEEE International Symposium on Broadband Multimedia Systems and Broadcasting (BMSB)*, pp. 1-5, Erlangen, Germany, 2011.
- [11] B. M. Isom, R. D. Palmer, G. S. Secrest, R. D. Rhoton, D. Saxion, T. L. Allmon, J. Reed, T. Crum, and R. Vogt, "Detailed Observations of Wind Turbine Clutter with Scanning Weather Radars", in *Journal of Atmospheric and Oceanic Technology*, vol. 26, no. 5, pp. 894-910, 2009.
- [12] K. V. Mishra and V. Chandrasekar, "Signal Analysis and Modeling of Wind Turbine Clutter in Weather Radars", in *Proceedings of the 2010 IEEE International Geoscience and Remote Sensing Symposium (IGARSS)*, pp. 3561-3564, 2010.
- [13] B. Gallardo-Hernando, J. M. Muñoz-Ferreras, F. Pérez-Martínez, and F. Aguado-Encabo, "Wind turbine clutter observations and theoretical validation for meteorological radar applications," *IET Radar, Sonar & Navigation*, vol. 5, no. 2, pp. 111-117, 2011.
- [14] J. Perry and A. Biss, "Wind farm clutter mitigation in air surveillance radar," *IEEE Aerospace and Electronics Systems Magazine*, vol. 22, no. 7, pp. 35-40, 2007.
- [15] A. Naqvi, S. Yang, and H. Ling, "Investigation of Doppler features from wind turbine scattering", *IEEE Antennas and Wireless Propagation Letters*, vol. 9, pp. 485-488, 2010.
- [16] A. Frye, "Theoretical and measurement results of the effects of wind turbines of military radar systems and technical assessment methods," in *Proceedings of the 60th IEA Topical Expert Meeting*, Senternovem, The Netherlands, November 2009.
- [17] I. Angulo, D. de la Vega, O. Grande, N. Cau, U. Gil, Y. Wu, D. Guerra, and P. Angueira, "Empirical evaluation of the impact of wind turbines on DVB-T reception quality," *IEEE Transactions on Broadcasting*, vol. 58, no. 1, pp. 1-9, 2012.

- [18] Meridian Energy Corp, *Application Documents of Project Hurunui Wind - Appendix N: Compatibility with Radio Services*, Meridian Energy Corp., Wellington, New Zealand, 2011.
- [19] A. Theil and J. van Ewijk, "Radar performance degradation due to the presence of wind turbines," in *Proceedings of the IEEE Radar Conference*, pp. 75-80, April 2007.
- [20] I. Angulo, D. Vega, O. Rodríguez, O. Grande, D. Guerra, and P. Angueira, "Analysis of the mast contribution to the scattering pattern of wind turbines in the UHF band," in *Proceedings of the 5th European Conference on Antennas and Propagation (EuCAP'11)*, pp. 707-711, 2011.
- [21] G. Greving and M. Malkomes, "Weather radar and wind turbines – an update of the theoretical and numerical analysis of effects," in *Proceedings of the 6th European Conference in Meteorology and Hydrology*, pp. 1-5, 2010.
- [22] S. Yang and H. Ling, "Electromagnetic Simulation of the Near-Field Distribution around a Wind Farm." *International Journal of Antennas and Propagation 2013*, Vol. 2013.
- [23] FEKO version 6.3, Stellenbosch, South Africa: EM Software & Systems Inc., 2013.
- [24] C. A. Balanis, *Advanced Engineering Electromagnetics*, 2/e, John Wiley & Sons, Hoboken, NJ, USA, 1989.
- [25] M. Leontovich and V. Fock, "Solution of propagation of electromagnetic waves along the Earth's surface by the method of parabolic equations," *Journal of Physics - USSR*, vol. 10, pp. 13-23, 1946.
- [26] M. Levy, *Parabolic equation methods for electromagnetic wave propagation*, London, IEE, Institution of Electrical Engineers, 2000.

- [27] A. Bamberge, B. Engquist, L. Halpern, and P. Joly, "Higher order paraxial wave equation approximations in heterogeneous media," *SIAM Journal on Applied Mathematics*, vol. 48, no. 1, pp. 129-154, 1988.
- [28] A. Arnold and M. Ehrhardt "Discrete transparent boundary conditions for wide angle parabolic equations in underwater acoustics," *Journal of Computational Physics*, vol. 145, no. 2, pp. 611-638, 1998.
- [29] A. Bamberger, B. Engquist, L. Halpern, and P. Joly, "Parabolic wave equation approximations in heterogeneous media," *SIAM Journal on Applied Mathematics*, vol. 48, no. 1, pp. 99-128, 1988.
- [30] J. Claerbout, *Fundamentals of Geophysical Data Processing: With Application to Petroleum Prospecting*, McGraw-Hill, New York, 1976.
- [31] C. Rappaport. "Perfectly matched absorbing boundary conditions based on anisotropic lossy mapping of space," *IEEE Microwave and Guided Wave Letters*, vol. 5, no. 3, pp. 90-92, 1995.
- [32] M. Levy and P. Borsboom, "Radar cross-section computations using the parabolic equation method", *IET Electronic Letters*, vol. 32, pp. 1234-1235, 1996.
- [33] M. Levy and P. Borsboom, A. Zaporozhets and A. Hyaric, "RCS calculations with the parabolic wave equation", in *AGARD Conference Proceedings*, Ankara, Turkey, no. 583, pp. 5.1-5.9, 1996.
- [34] P. Borsboom and A. Hyaric, "RCS predictions using wide-angle PE codes", in *Proceedings of 10<sup>th</sup> International Conference of Antenna and Propagation*, no. 436, pp. 2.191-2.194, 1997.
- [35] *Channel Analysis Tool (CAT) Use Guide Version 1.0*, Time Domain Corporation.